
Mixed-Curvature Decision Trees and Random Forests

Philippe Chlenski¹ Quentin Chu¹ Raiyan R Khan¹ Kaizhu Du¹ Antonio Khalil Moretti^{2,3} Itsik Pe'er¹

Abstract

Decision trees (DTs) and their random forest (RF) extensions are workhorses of classification and regression in Euclidean spaces. However, algorithms for learning in non-Euclidean spaces are still limited. We extend DT and RF algorithms to product manifolds: Cartesian products of several hyperbolic, hyperspherical, or Euclidean components. Such manifolds handle heterogeneous curvature while still factorizing neatly into simpler components, making them compelling embedding spaces for complex datasets. Our novel angular reformulation of DTs respects the geometry of the product manifold, yielding splits that are geodesically convex, maximum-margin, and composable. In the special cases of single-component manifolds, our method simplifies to its Euclidean or hyperbolic counterparts, or introduces hyperspherical DT algorithms, depending on the curvature. We benchmark our method on various classification, regression, and link prediction tasks on synthetic data, graph embeddings, mixed-curvature variational autoencoder latent spaces, and empirical data. Compared to 7 other classifiers, product RFs ranked first on 25 out of 57 benchmarks, and placed in the top 2 for 46 out of 57. This highlights the value of product RFs as straightforward yet powerful new tools for data analysis in product manifolds. Code for our paper is available at <https://github.com/pchlenski/manifold>.

1. Introduction

While much of machine learning focuses on Euclidean spaces, these can fail to capture the true structure of complex datasets. For example, hierarchical structures, which are common in taxonomy (e.g., phylogenetic trees) are better represented in hyperbolic space due to its exponential volume growth, which naturally mirrors tree-like data (Sonthalia & Gilbert, 2020). Similarly, cyclical structures, often encountered in time-series data with periodic patterns (e.g., seasonal trends, neuronal spiking dynamics), can benefit from spherical representations (Ding & Regev, 2021).

However, many real-world datasets don't conform to a single geometric structure. Any constant-curvature manifold—whether hyperbolic, spherical, or Euclidean—would struggle to represent all the nuances of such data simultaneously. Product manifolds, as proposed by Gu et al. (2018), offer a solution. By combining multiple constant-curvature component manifolds (spherical, Euclidean, and hyperbolic spaces) into a single product manifold, they can better capture the complexity of such mixed-structure data. This flexibility reduces distortion when modeling pairwise distances and enables a more accurate representation of the underlying data structure.

Despite their advantages, product manifolds have seen limited adoption in machine learning, particularly for inference tasks like classification and regression. Existing work has primarily focused on applications in biology (McNeela et al., 2024) and knowledge graphs (Wang et al., 2021). However, tools for leveraging product manifold representations in downstream tasks remain scarce.

In this paper, we introduce mixed-curvature decision trees (DTs) and random forests (RFs), expanding the toolkit for analyzing product manifold data. By enabling inference directly on product manifold coordinates, our approach is well-suited for datasets that combine hierarchical, cyclical, and other complex geometric patterns. This framework provides a principled way to learn from such structures, achieving more accurate results than competing models. These contributions offer new possibilities for applying product manifold representations in fields ranging from biological modeling to temporal-spatial analysis.

Our contributions:

1. We generalize DTs and RFs to *all* constant-curvature manifolds. Unlike existing methods, we represent data and splits as angles in two-dimensional subspaces. This guarantees splits are geodesically convex, maximum-margin, and composable. For single manifolds, this extends existing Euclidean and hyperbolic models or introduces *hyperspherical* DTs and RFs.
2. We introduce novel DT and RF algorithms for product manifolds.
3. We extend techniques for sampling distributions in non-Euclidean manifolds to describe mixtures of Gaussians in product manifolds.

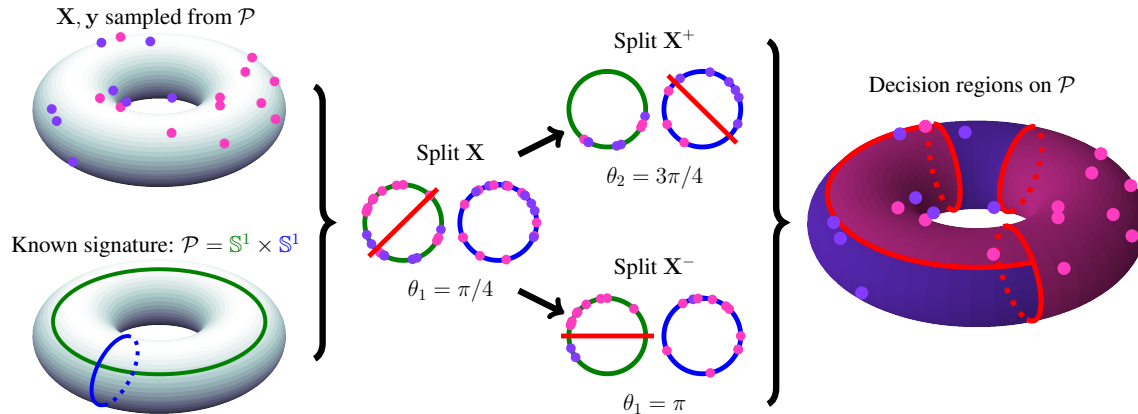


Figure 1: An illustration of the product manifold DT in action. We consider a sample of labeled points (\mathbf{X}, \mathbf{y}) from one of the simplest possible product manifolds: the torus $\mathcal{P} = \mathbb{S}^1 \times \mathbb{S}^1$. Since we know the signature for \mathcal{P} , we can factorize \mathbf{X} into coordinates on two circles. Our DT **splits** these factorized coordinates to a maximum depth of 2, partitioning \mathcal{P} into a total of $2^2 = 4$ disjoint decision areas (colored **positive** or **negative** to reflect the classes).

4. We show how problems like link prediction in graphs and signal analysis can be recast as inference problems on product manifolds.
5. We demonstrate the effectiveness of our algorithms against a variety of baselines on a diverse suite of 57 non-Euclidean benchmarks.

1.1. Related work

Non-Euclidean representation learning. Important background on manifolds in machine learning is given in Cayton (2005) and Bengio et al. (2014). Much of the work on product manifolds is indebted to early works on hyperbolic spaces, including Nickel & Kiela (2017); Chamberlain et al. (2017), and Ganea et al. (2018).

Machine learning in product manifolds. Tabaghi et al. (2021) describe linear classifiers, including perceptron and support vector machines; Tabaghi et al. (2024) adapt principal component analysis; and Cho et al. (2023) generalize Transformer architectures to product manifolds.

Product manifold-derived features. Sun et al. (2021) and Borde et al. (2023b) use product manifolds to compute rich similarity measures as features for classification. Giovanni et al. (2022) introduce a heterogeneous variant of product manifolds; Borde et al. (2024) combine quasi-metrics and partial orders for graph representation.

Manifold random forests. Our method is inspired by recent work by Doorenbos et al. (2023) and Chlenski et al. (2024) extending RFs to hyperbolic space. Other work has explored generalizations of random forests to manifolds, including random forest regression for manifold-valued *targets* (Tsagkrasoulis & Montana, 2017), manifold

oblique random forests (Li et al., 2022), and Fréchet random forests (Capitaine et al., 2024).

Applications of product manifolds. Product manifolds are popular for embedding knowledge graphs (Wang et al., 2021; Nguyen-Van et al., 2023; Li et al., 2024). In biology, they have been used to represent pathway graphs (McNeela et al., 2024), cryo-EM images (Zhang et al., 2021), and single-cell transcriptomic profiles (Tabaghi et al., 2021). Skopek et al. (2020) also embed image datasets into product manifolds.

2. Preliminaries

We review relevant details of different Riemannian manifolds (Euclidean spaces, hyperspheres, hyperboloids, and product manifolds), along with key properties of the Euclidean and hyperbolic variants of DTs and RFs.

2.1. Riemannian manifolds

We will begin by reviewing key details of hyperspheres, hyperboloids, and Euclidean spaces. For more details, readers can consult Do Carmo (1992).

Each space described is a Riemannian manifold, meaning that it is locally isomorphic to Euclidean space and equipped with a distance metric. The shortest paths between two points \mathbf{u} and \mathbf{v} on a manifold are called geodesics. As all three spaces we consider have constant Gaussian curvature, we define simple closed forms for geodesic distances in each of the following subsections in lieu of a more general discussion of geodesics in arbitrary Riemannian manifolds.

Any constant-curvature manifold \mathcal{M} is parameterized by a

dimensionality D and a curvature K . They can also all be considered embedded in an ambient space \mathbb{R}^{D+1} . Finally, for each point $\mathbf{x} \in \mathcal{M}$, the tangent plane at \mathbf{x} , $T_{\mathbf{x}}\mathcal{M}$, is the space of all tangent vectors at \mathbf{x} :

$$T_{\mathbf{x}}\mathcal{M} = \{\mathbf{x}' \in \mathcal{M} : \langle \mathbf{x}', \mathbf{x} \rangle_{\mathcal{M}} = 0\}. \quad (1)$$

2.1.1. EUCLIDEAN SPACE

Euclidean spaces are naturally understood as \mathbb{R}^D , but we will use the notation $\mathbb{E}^D = \mathbb{R}^D$ when treating Euclidean spaces as manifolds. In contrast, we will continue to use \mathbb{R}^D to refer to ambient spaces. Euclidean spaces use the familiar inner product (dot product), norm (ℓ_2 norm), and distance function (Euclidean distance):

$$\langle \mathbf{u}, \mathbf{v} \rangle = u_0v_0 + u_1v_1 + \dots + u_{D-1}v_{D-1}, \quad (2)$$

$$\|\mathbf{u}\| = \sqrt{\langle \mathbf{u}, \mathbf{u} \rangle}, \quad (3)$$

$$\delta_{\mathbb{E}}(\mathbf{u}, \mathbf{v}) = \|\mathbf{u} - \mathbf{v}\|. \quad (4)$$

2.1.2. HYPERSPHERICAL SPACE

Hyperspheres can be viewed as surfaces *embedded* in a higher-dimensional, Euclidean ambient space. Hyperspherical space uses the same inner products as Euclidean space. The hypersphere is the set of points in the ambient space having a Euclidean norm equal to some radius inversely proportional to the curvature $K > 0$:

$$\mathbb{S}^{D,K} = \{\mathbf{x} \in \mathbb{R}^{D+1} : \|\mathbf{x}\| = 1/K\}. \quad (5)$$

Because shortest paths between two points \mathbf{u} and \mathbf{v} in $\mathbb{S}^{D,K}$ through the ambient space leave the surface of the manifold, we must define the hyperspherical distance function for the shortest path entirely in $\mathbb{S}^{D,K}$ between \mathbf{u} and \mathbf{v} :

$$\delta_{\mathbb{S}}(\mathbf{u}, \mathbf{v}) = \cos^{-1}(K^2 \langle \mathbf{u}, \mathbf{v} \rangle) / K. \quad (6)$$

2.1.3. HYPERBOLIC SPACE

Hyperbolic space is characterized by constant negative metric curvature. This has several consequences: for instance, the angles in any triangle sum to less than π , many lines through a point can be parallel to any given line, and neighborhoods grow exponentially with radius.

There are several equivalent models of hyperbolic space. For our purposes, we will describe the hyperbolic space from the perspective of the hyperboloid model. First, we must define the ambient Minkowski space. This is a vector space equipped with the Minkowski inner product:

$$\langle \mathbf{u}, \mathbf{v} \rangle_{\mathcal{L}} = -u_0v_0 + u_1v_1 + \dots + u_nv_n. \quad (7)$$

Similar to the Euclidean case, we let $\|\mathbf{u}\|_{\mathcal{L}} = \langle \mathbf{u}, \mathbf{u} \rangle_{\mathcal{L}}$ (we do not wish to take the square root of a negative number).

The hyperboloid of dimension D and curvature $K < 0$, written $\mathbb{H}^{D,K}$, is a set of points with constant Minkowski norm:

$$\mathbb{H}^{D,K} = \{\mathbf{x} \in \mathbb{R}^D : \|\mathbf{x}\|_{\mathcal{L}} = -1/K^2, x_0 > 0\}, \quad (8)$$

Finally, the hyperbolic distance function for geodesic distances between $\mathbf{u}, \mathbf{v} \in \mathbb{H}^{D,K}$ is given by

$$\delta_{\mathbb{H}}(\mathbf{u}, \mathbf{v}) = -\cosh^{-1}(K^2 \langle \mathbf{u}, \mathbf{v} \rangle_{\mathcal{L}}) / K. \quad (9)$$

2.1.4. MIXED-CURVATURE PRODUCT MANIFOLDS

We reiterate the definition of product manifolds from Gu et al. (2018). Following the convention of using $\prod_i \mathbf{X}_i$ to refer to the iterated *Cartesian* product over sets, the product manifold is defined as

$$\mathcal{P} = \prod_{i=1}^n \mathbb{S}^{s_i, K_i} \times \prod_{j=1}^m \mathbb{H}^{h_j, K'_j} \times \mathbb{E}^d. \quad (10)$$

The total number of dimensions is $\sum_i^n s_i + \sum_j^m h_j + d$. Each individual manifold is called a component manifold, and the decomposition of the product manifold into component manifolds is called the signature. Informally, the signature can be considered a list of dimensionalities and curvatures for each component manifold.

Distances in \mathcal{P} decompose as the ℓ_2 norm of the distances in each of the component manifolds:

$$\delta_{\mathcal{P}}(\mathbf{u}, \mathbf{v}) = \sqrt{\sum_{\mathcal{M} \in \mathcal{P}} \delta_{\mathcal{M}}(\mathbf{u}_{\mathcal{M}}, \mathbf{v}_{\mathcal{M}})^2}, \quad (11)$$

where $\mathbf{u}_{\mathcal{M}}$ and $\mathbf{v}_{\mathcal{M}}$ denotes the restriction of \mathbf{u} and \mathbf{v} to their components in \mathcal{M} and $\delta_{\mathcal{M}}$ refers the distance function appropriate to \mathcal{M} .

For $\mathbf{x} \in \mathcal{P}$, the tangent plane at \mathbf{x} , $T_{\mathbf{x}}\mathcal{P}$, is the direct sum (concatenation) of all component tangent planes:

$$T_{\mathbf{x}}\mathcal{P} = \bigoplus_{\mathcal{M} \in \mathcal{P}} T_{\mathbf{x}_{\mathcal{M}}}\mathcal{M}. \quad (12)$$

We additionally define the origin of \mathcal{P} , μ_0 , as the concatenation of the origins of each respective manifold. The origin is $(1/|K|, 0, \dots)$ for $\mathbb{H}^{D,K}$ and $\mathbb{S}^{D,K}$, and $(0, 0, \dots)$ for \mathbb{E}^D .

2.2. Decision trees and random forests

The Classification and Regression Trees (CART) (Breiman, 2017) algorithm fits a DT \mathcal{T} to a set of labeled data (\mathbf{X}, \mathbf{y}) . At each step, it greedily selects the split which partitions the dataset with maximum information gain,

$$\text{IG}(\mathbf{y}) = C(\mathbf{y}) - \frac{|\mathbf{y}^+|}{|\mathbf{y}|} C(\mathbf{y}^+) - \frac{|\mathbf{y}^-|}{|\mathbf{y}|} C(\mathbf{y}^-). \quad (13)$$

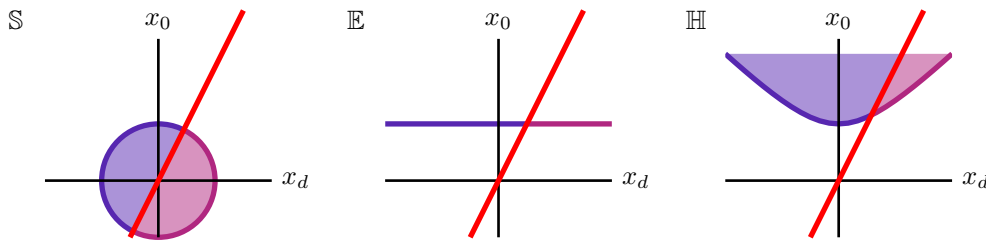


Figure 2: Decision boundaries in any constant-curvature manifold are found by 2-D projections into 2-dimensional subspaces. In this perspective, both data and splits are parameterized by an angle θ . Each **split** divides the manifold into **positive-class regions** and **negative-class regions**.

Here, $C(\cdot)$ is some impurity function (we use Gini impurity for classification and variance for regression). A splitting function $S(\cdot)$ partitions the *labels* \mathbf{y} into two classes, \mathbf{y}^+ and \mathbf{y}^- and the *input space* into decision regions. Classically, $S(\cdot)$ is a thresholding function that partitions the input space into high-dimensional boxes given a dimension d and threshold θ :

$$S(\mathbf{x}) = \mathbb{I}\{x_d > \theta\}. \quad (14)$$

This algorithm is applied recursively to each decision region until a stopping condition is met (e.g., maximum number of splits is reached). The result is a fitted DT, \mathcal{T} , which can be used for inference. During inference, an unseen point \mathbf{x} is passed through \mathcal{T} until it reaches a leaf node corresponding to some decision region. For classification, the point is then assigned the majority label inside that region; for regression, it is assigned the mean value inside that region.

Finally, a RF is an ensemble of DTs, typically trained on a bootstrapped subsample of the points and features in \mathbf{X} (Breiman, 2001).

2.2.1. HYPERBOLIC DECISION TREE ALGORITHMS

The hyperplane perspective on DTs is helpful background for understanding our method: mathematically, thresholding \mathbf{x} on a dimension is equivalent to taking its dot product with the normal vector of a separating hyperplane \mathbb{P} , even in hyperbolic space. Although this is easy to compute for classical thresholding boundaries, which are zero in all dimensions but d , this perspective principally admits *any hyperplane* \mathbb{P} as a valid decision boundary.

Naturally, considerations around choosing an appropriate (and computationally efficient) \mathbb{P} abound. To this end, Chlenski et al. (2024) impose homogeneity and sparsity constraints on the hyperplanes they consider for hyperbolic DTs. In hyperbolic space, homogenous hyperplanes—hyperplanes that contain the origin of the ambient space—intersect $\mathbb{H}^{D,K}$ at geodesic submanifolds: that is, $\mathbb{P} \cap \mathbb{H}^{D,K}$ is closed under shortest paths according to $\delta_{\mathbb{H}}$. The sparsity

constraint enforces that the normal vectors of \mathbb{P} must be nonzero only in two positions: the timelike coordinate x_0 and some other x_d , which ensures that only $\mathcal{O}(nd)$ candidate hyperplanes are considered per split, and each decision can be computed in $\mathcal{O}(1)$ time using sparse dot products.

3. Mixed-curvature decision trees

For any DT, we must transform the input \mathbf{X} into a set of candidate hyperplanes. To this end, we reframe and generalize the hyperplane approach of hyperbolic DTs. First, we observe that homogenous hyperplanes are geodesically convex in *any constant-curvature manifold*; therefore, we can extend the hyperbolic DT approach to \mathbb{E} and \mathbb{S} . Second, we observe that fitting sparse, homogenous DTs is equivalent to thresholding on angles under 2-dimensional projections.

We consider the set of all projections onto the basis $\{x_0, x_d\}$, which are computable in $\mathcal{O}(1)$ time per projection by coordinate selection. First, we compute the projection angle:¹

$$\theta(\mathbf{x}, d) = \tan^{-1}(x_0/x_d). \quad (15)$$

Next, we use a modified splitting criterion to account for the geometry of angular splits:

$$S(\mathbf{x}, d, \theta) = \mathbb{I}\{\theta(\mathbf{x}, d) \in [\theta, \theta + \pi)\}. \quad (16)$$

Once the best angle is selected, we must compute angular midpoints to select \mathbb{P} that intersects \mathcal{M} at a point *geodesically equidistant* the two points to either side of it (Euclidean DTs do this by sampling averaging the threshold values). Angular midpoints for each component manifold are described in the following sections and summarized in Table 5 in the Appendix.

With the angular features and manifold-informed midpoint modifications in place, the rest of the algorithm follows Section 2.2 unmodified.

¹We use the PyTorch `arctan2` function to ensure that we can recover the full range of angles in $[0, 2\pi)$. This is essential for properly specifying decision boundaries in \mathbb{S} .

3.1. Euclidean decision trees

While the intersections of homogenous hyperplanes in \mathbb{R}^D with \mathbb{E}^D are (trivially) convex, these lack the expressiveness of an ambient-space formulation. Thus, we embed \mathbb{E}^D in \mathbb{R}^{D+1} by a trivial lift:

$$\phi : \mathbb{E}^D \rightarrow \mathbb{R}^{D+1}, \phi(\mathbf{u}) = (1, \mathbf{u}). \quad (17)$$

For two points $\mathbf{u}, \mathbf{v} \in \mathbb{E}^D$, the midpoint angles in \mathbb{E}^D can be described in terms of the coordinates of \mathbf{u} and \mathbf{v} or their respective projection angles (θ_u, θ_v) as

$$m_{\mathbb{E}}(\mathbf{u}, \mathbf{v}) = \tan^{-1}(2/(u_d + v_d)) \quad (18)$$

$$= \tan^{-1} \left(\frac{\tan^{-1}(\theta_u) \tan^{-1}(\theta_v)}{\tan^{-1}(\theta_u) + \tan^{-1}(\theta_v)} \right). \quad (19)$$

While this presentation of Euclidean DTs is unconventional, it is completely equivalent to thresholding in the basis dimensions. See Appendix C for the proof.

3.2. Hyperbolic decision trees

For two points $\mathbf{u}, \mathbf{v} \in \mathbb{H}^{D,K}$, we compute θ_u and θ_v according to Eq 15 and follow Chlenski et al. (2024) in computing the hyperbolic midpoint angle in $\mathbb{H}^{D,K}$ as:

$$V := \frac{\sin(2\theta_u - 2\theta_v)}{\sin(\theta_u + \theta_v) \sin(\theta_v - \theta_u)}, \quad (20)$$

$$m_{\mathbb{H}}(\mathbf{u}, \mathbf{v}) = \begin{cases} \cot^{-1}(V - \sqrt{V^2 - 1}) & \text{if } \theta_u + \theta_v < \pi \\ \cot^{-1}(V + \sqrt{V^2 - 1}) & \text{otherwise.} \end{cases} \quad (21)$$

3.3. Hyperspherical decision trees

The hyperspherical case is quite simple, except that unlike hyperbolic space and the “lifted” Euclidean space after applying Eq 17, we lack a natural choice of x_0 . We adopt the convention of fixing the first dimension of the embedding space as x_0 , which intuitively corresponds to fixing a “north pole” at the origin $\mu_0 = (1/|K|, 0, \dots)$.

Angular midpoints are particularly well-behaved in hyperspherical manifolds: given $\mathbf{u}, \mathbf{v} \in \mathbb{S}^{D,K}$, the hyperspherical midpoint angle by finding θ_u and θ_v using Eq 15 and taking their mean:

$$m_{\mathbb{S}}(\mathbf{u}, \mathbf{v}) = (\theta_u + \theta_v)/2. \quad (22)$$

3.4. Product decision tree algorithm

Intuitively, the transition from DTs in a single component manifold to a product manifold is that we now iterate over all preprocessed angles together, using the angular midpoint formula appropriate to each component. The complete pseudocode for this algorithm is in Appendix B.

Letting a single DT to span all components—as opposed to an ensemble of DTs, each operating in a single component—allows the model to independently allocate its splits across components according to their relevance to the task at hand. Recasting DT learning in terms of angular comparisons has three major advantages over finding planar decision boundaries directly:

1. We can consider angles under *arbitrary* linear projections (not just projections onto basis dimensions) while maintaining $\mathcal{O}(1)$ decision complexity.
2. It becomes possible to subsample the features (pre-computed angles) as is typical in RFs.
3. Product manifolds can always represent additional features in a new Euclidean manifold.

4. Benchmarks

We carried out benchmarks to evaluate which model, given a labeled set of mixed-curvature embeddings, achieves the lowest error on a test set. While we produced embeddings using a range of datasets and embedding techniques, our results focus only on performance on downstream tasks. We describe our data generation/embedding methods in more detail in Appendix Section E.

We summarize our benchmark results, with references to specific figures and tables, in Table 1.

Table 1: Benchmarks summary. The “Task” column is C (Classification), R (Regression), or LP (Link prediction). “#Top- k ” columns count how often product DTs or RFs were among the top k predictors for a given set of benchmarks.

Manifold	Task	Ref	#Top-1	#Top-2	Total
Single	C	Fig. 3	7	11	11
Single	R	Fig. 4	7	9	11
Product	C	Tab. 2	5	13	18
Product	R	Tab. 3	5	9	11
Product	LP	Tab. 4	1	4	6
Total			25	46	57

4.1. Experiment details

Problem setup. Given a dataset \mathbf{X} , a set of labels \mathbf{y} , and a product manifold \mathcal{P} , we evaluate a variety of classifiers on their ability to predict \mathbf{y} from \mathbf{X} . We apply an identical 80:20 train-test split to all of our data, train our models on the training set, and evaluate performance on the test set. We report 95% confidence intervals for accuracy scores for classification, root mean squared error (RMSE) for regression, and accuracy scores again for link prediction benchmarks.

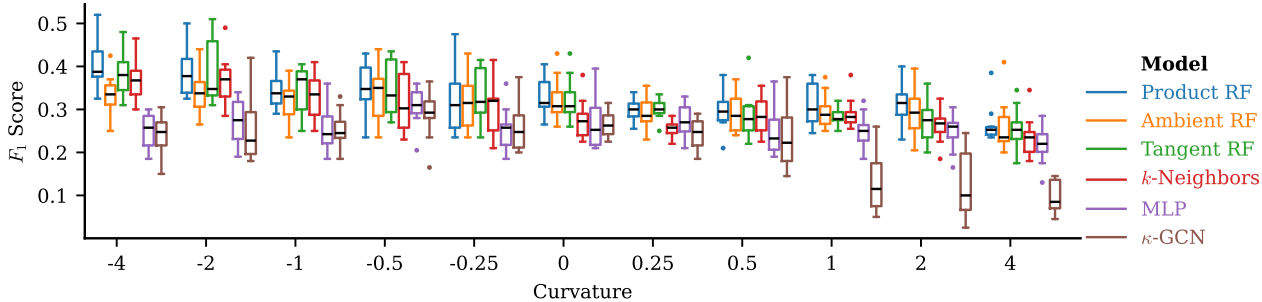


Figure 3: Single-curvature classification benchmark. We report micro-averaged F_1 scores on a synthetic data classification task involving mixtures of 8 Gaussians in manifolds of varying constant curvatures K . We omit product space perceptrons, ambient-space GNNs, and geodesic MLR, which never achieved competitive results

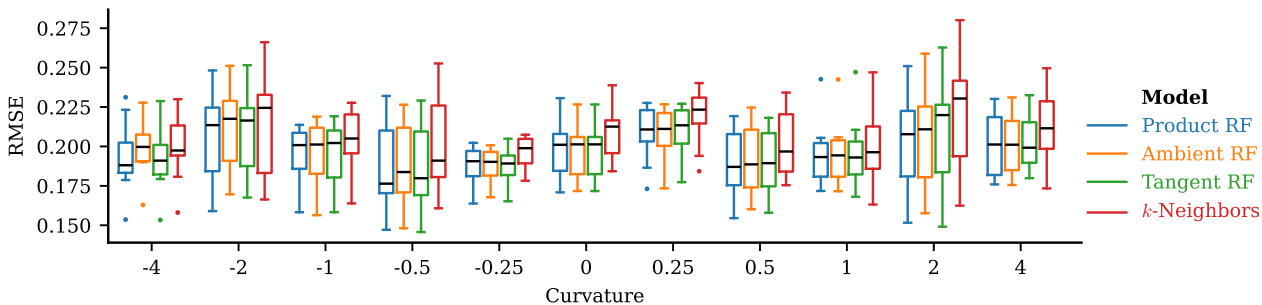


Figure 4: Regression benchmarks (RMSE) for single-curvature manifolds. We follow the conventions of Figure 3. Results for product space perceptrons and all neural networks are significantly worse and, therefore, omitted from the plot.

4.2. Datasets

Synthetic data. We develop a novel method to sample mixtures of Gaussians in \mathcal{P} to generate classification and regression datasets. For classification, we generate 8 classes using 32 clusters. For regression, we generate a single scalar response variable using 32 clusters with randomly-generated intercepts. For more details, see Appendix Section A.

Graph embeddings. For classification and regression on graph datasets, we generate embeddings that approximate shortest-path distances in the graph using the method described in Gu et al. (2018). We select the optimal signature from the candidate set $\{(\mathbb{H}^2)^2, \mathbb{H}^2\mathbb{E}^2, \mathbb{H}^2\mathbb{S}^2, \mathbb{S}^2\mathbb{E}^2, (\mathbb{S}^2)^2, \mathbb{H}^4, \mathbb{E}^4, \mathbb{S}^4\}$ by generating embeddings in each signature and selecting the signature with the lowest metric distortion. For link prediction, we embed all datasets in $\mathcal{P} = (\mathbb{S}^2\mathbb{E}^2\mathbb{H}^2)$, then create a binary classification dataset by associating each pair of nodes with a point in $\mathcal{P}^2\mathbb{E}^1$, where each pair of points is included and the last Euclidean dimension is the manifold distance $\delta_{\mathcal{P}}(\mathbf{x}_i, \mathbf{x}_j)$; labels are simply whether there is an edge between nodes i and j . Full details on graph embeddings are described in Appendix Section E.4.

Mixed-curvature VAE latent space. We follow Skopek et al. (2020) in training variational autoencoders (VAEs) whose latent space is \mathcal{P} . Once the VAE is trained, we use its encoder to generate embeddings for our dataset and classify these embeddings. Full details on VAE training and downstream inference are described in Appendix Section E.5.

Empirical datasets. Some datasets can be represented in a non-Euclidean geometry without generating embeddings: for instance, geospatial data lives in \mathbb{S}^2 , while cyclic time series embed in \mathbb{S}^1 . We describe our approach to generating embeddings for these empirical datasets in Appendix E.6.

4.3. Baselines

We use Scikit-Learn (Pedregosa et al., 2011) DTs and RFs in both the ambient space \mathbb{R}^{D+1} and the tangent plane $T_{\mu_0}\mathcal{P}$: Ambient space models operate directly on ambient space coordinates. Tangent plane models project points from \mathcal{P} to $T_{\mu_0}\mathcal{P}$ by applying the logarithmic map at μ_0 as a pre-processing step. We use Scikit-Learn k -nearest neighbor (k -NN) classifiers and regressors with precomputed pairwise distance matrices according to $\delta_{\mathcal{P}}$ (Eq. 11). We also implemented the product space perceptron algorithm described

Mixed-Curvature Decision Trees and Random Forests

Table 2: Accuracies for all product manifold classification benchmarks. The highest scores for each dataset are shown in **bold**, while second-best predictors are underlined. For brevity, we omit columns for three low-performing methods: product space perceptrons, ambient-space GNNs, and product space MLR.

	Dataset	Signature	Product RF	Ambient RF	Tangent RF	k -Neighbors	Ambient MLP	κ -GCN
Synthetic (multi- K)	Gaussian	$(\mathbb{S}^2)^2$	36.8 ± 1.2	35.4 ± 1.5	35.7 ± 1.4	<u>36.6 ± 1.6</u>	30.5 ± 1.4	14.4 ± 2.5
		\mathbb{E}^4	36.9 ± 1.4	37.2 ± 1.8	37.2 ± 1.8	36.6 ± 1.3	30.6 ± 1.5	26.3 ± 2.3
		$\mathbb{H}^2\mathbb{E}^2$	41.2 ± 2.0	38.6 ± 2.1	39.1 ± 1.8	<u>39.8 ± 2.3</u>	32.2 ± 2.0	25.2 ± 1.6
		$\mathbb{H}^2\mathbb{S}^2$	<u>37.6 ± 1.7</u>	<u>37.6 ± 2.0</u>	37.1 ± 1.9	38.1 ± 2.5	32.0 ± 1.7	14.8 ± 2.4
		\mathbb{H}^4	<u>45.2 ± 2.3</u>	39.2 ± 1.6	41.4 ± 1.5	45.3 ± 1.6	33.5 ± 2.1	25.0 ± 2.6
		$\mathbb{S}^2\mathbb{E}^2$	<u>37.2 ± 1.3</u>	36.6 ± .9	37.3 ± 1.4	35.9 ± 1.3	29.7 ± 1.1	22.0 ± 2.5
		\mathbb{S}^4	<u>28.3 ± 1.1</u>	24.9 ± .9	25.8 ± 1.0	30.2 ± .8	19.9 ± 1.2	17.4 ± .5
		<u>$(\mathbb{H}^2)^2$</u>	<u>39.6 ± 1.5</u>	37.7 ± 1.0	38.7 ± 1.2	40.5 ± 1.0	31.5 ± 1.9	24.3 ± 1.7
Graphs	CiteSeer	$\mathbb{H}^2\mathbb{S}^2$	26.2 ± .7	25.5 ± .8	<u>25.9 ± .7</u>	25.1 ± .5	24.5 ± .7	23.8 ± .5
	Cora	\mathbb{H}^4	29.2 ± .5	29.7 ± .4	29.3 ± .4	20.8 ± .4	29.9 ± .5	<u>29.7 ± .5</u>
	PolBlogs	$(\mathbb{S}^2)^2$	93.4 ± .4	93.1 ± .5	93.9 ± .6	92.9 ± .4	91.7 ± .4	91.5 ± .7
VAE	Blood	$\mathbb{S}^2\mathbb{E}^2(\mathbb{H}^2)^3$	16.0 ± 1.2	18.4 ± .8	<u>18.3 ± .7</u>	15.9 ± .6	12.0 ± .4	11.3 ± .4
	CIFAR-100	$(\mathbb{S}^2)^4$	10.3 ± .6	<u>10.4 ± .5</u>	10.6 ± .6	7.9 ± .5	8.1 ± .4	4.9 ± .3
	Lymphoma	$(\mathbb{S}^2)^2$	84.8 ± 1.1	<u>82.4 ± 1.2</u>	82.1 ± 1.2	78.5 ± 1.3	78.4 ± .3	73.0 ± 5.6
	MNIST	$\mathbb{S}^2\mathbb{E}^2\mathbb{H}^2$	35.1 ± 4.4	<u>37.6 ± 3.2</u>	38.8 ± 3.2	35.0 ± 4.3	35.2 ± 3.9	11.3 ± 1.1
Other	Landmasses	\mathbb{S}^2	87.4 ± .9	85.9 ± .9	84.6 ± .8	91.8 ± .6	69.9 ± .8	71.4 ± 1.7
	Neuron 33	$(\mathbb{S}^1)^{10}$	<u>77.5 ± 1.4</u>	78.6 ± 1.2	76.6 ± 1.6	50.8 ± 1.6	46.1 ± 1.4	48.9 ± 1.8
	Neuron 46	$(\mathbb{S}^1)^{10}$	62.0 ± 1.2	<u>61.8 ± .9</u>	60.6 ± 1.1	49.0 ± 1.5	48.1 ± 1.1	48.0 ± 1.0

Table 3: Regression performance (RMSE) for all product manifold classification benchmarks. Following the conventions of Table 2, we emphasize high-scoring predictors and omit columns for predictors that never achieve the highest score. CS PhDs is a graph embedding dataset, whereas Temperature and Traffic are empirical.

	Dataset	Signature	Product RF	Ambient RF	Tangent RF	k -Neighbors
Synthetic (multi- K)	Gaussian	$(\mathbb{S}^2)^2$.192 ± .006	<u>.194 ± .007</u>	<u>.194 ± .007</u>	.200 ± .006
		\mathbb{E}^4	.191 ± .005	.191 ± .005	.191 ± .005	.195 ± .005
		$\mathbb{H}^2\mathbb{E}^2$.201 ± .006	.198 ± .006	<u>.200 ± .006</u>	.205 ± .006
		$\mathbb{H}^2\mathbb{S}^2$.192 ± .007	<u>.192 ± .007</u>	.189 ± .007	.197 ± .008
		\mathbb{H}^4	.183 ± .006	.186 ± .006	<u>.185 ± .006</u>	.187 ± .006
		$\mathbb{S}^2\mathbb{E}^2$	<u>.188 ± .012</u>	.187 ± .013	<u>.188 ± .012</u>	.193 ± .012
		\mathbb{S}^4	.176 ± .005	<u>.178 ± .004</u>	<u>.178 ± .004</u>	.181 ± .005
		<u>$(\mathbb{H}^2)^2$</u>	<u>.174 ± .007</u>	<u>.176 ± .006</u>	<u>.176 ± .006</u>	.177 ± .007
Other	CS PhDs	\mathbb{H}^4	13.986 ± .629	14.001 ± .687	14.123 ± .697	13.135 ± .497
	Temperature	$\mathbb{S}^2\mathbb{S}^1$	<u>8.128 ± .682</u>	5.506 ± .821	8.841 ± .579	11.590 ± .628
	Traffic	$(\mathbb{S}^1)^4\mathbb{E}^1$.549 ± .012	.470 ± .011	<u>.474 ± .009</u>	.503 ± .010

Table 4: Accuracies for all link prediction benchmarks, also following the conventions in Table 2. The κ -GCN is trained using a conventional link prediction approach; the other classifiers are trained as binary classifiers on the product of input embeddings \mathbf{X}^2 . All graphs were embedded into $\mathbb{H}^2\mathbb{E}^2\mathbb{S}^2$.

Dataset	Product RF	Ambient RF	Tangent RF	k -Neighbors	Ambient MLP	κ -GCN
AdjNoun	92.5 ± .5	<u>92.5 ± .5</u>	<u>92.5 ± .5</u>	92.1 ± .5	92.6 ± .5	92.5 ± .5
Dolphins	91.7 ± .3	<u>91.7 ± .4</u>	<u>91.7 ± .3</u>	91.4 ± .3	91.6 ± .3	91.8 ± .2
Football	79.5 ± .8	79.1 ± .7	<u>79.3 ± .8</u>	77.9 ± .8	79.1 ± .7	51.6 ± 7.9
Karate Club	87.4 ± .8	88.3 ± .7	87.7 ± .8	87.1 ± 1.4	85.5 ± .6	86.1 ± 1.1
Les Mis	91.9 ± .2	<u>92.7 ± .5</u>	92.5 ± .5	93.5 ± .3	91.7 ± .2	91.0 ± .3
PolBooks	<u>91.6 ± .6</u>	<u>91.6 ± .6</u>	91.8 ± .6	91.0 ± .8	<u>91.6 ± .6</u>	<u>91.6 ± .6</u>

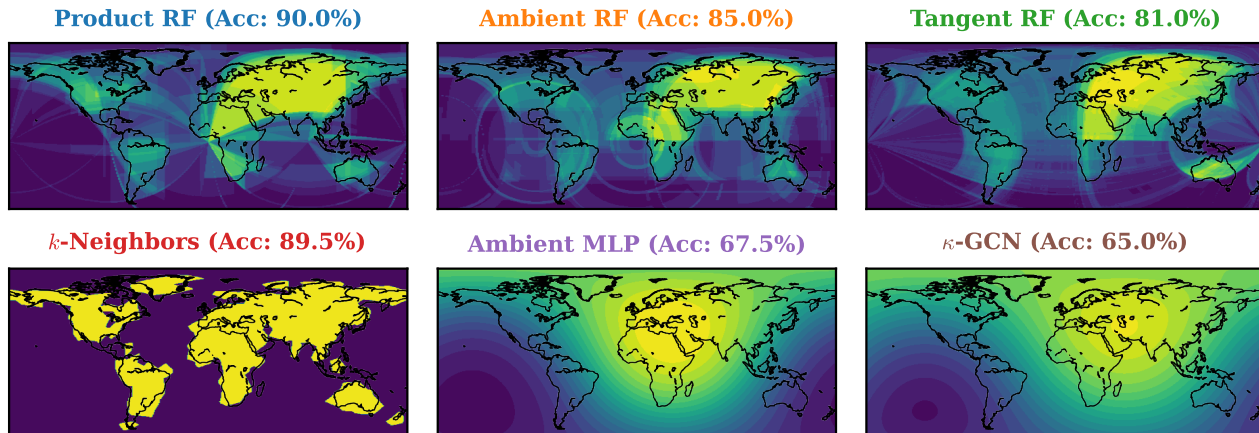


Figure 5: We color a world map with each model’s predicted $\mathbb{P}(\text{Land})$ for the “Landmasses” dataset, a land vs. water classification benchmark in \mathbb{S}^2 . Each RF consists of 12 DTs with a max depth of 5. Note the artifacts learned by **Euclidean RFs**, **tangent RFs**, and **k -Neighbors**, as well as the diffuse probabilities learned by the **ambient MLP** and **κ -GCN**.

in Tabaghi et al. (2021). Finally, we implement multilayer perceptron (MLP) and graph convolutional network (GCN) models in the ambient space and in product manifolds using our own implementation of the κ -GCN model described in Bachmann et al. (2020).

For our own models, we set hyperparameters identically to Scikit-Learn DTs and RFs, except we consider all $\binom{D}{2}$ projections—for a total of 3 features per 2-dimensional component manifold, just like ambient space methods use. Full details for each model can be found in Appendix E.2.

4.4. Results

For single-curvature synthetic datasets, our method was the best classifier in 7 out of 11 signatures (Figure 3) and the best regressor (Figure 4) for 7 out of 11 signatures. In Tables 2, 3, and 4, we demonstrate consistently good performance across a diverse range of benchmarks. Across a series of challenging benchmarks, our method is the best for 25 out of 57 cases (44%), and is in the top-2 best for 46 out of 57 cases (81%).

Further experiments can be found in the Appendix: we provide ablations in Appendix F, detailed tables and latent space visualizations in Appendix G, runtime and computational complexity analysis in Appendix H, and interpretability experiments in Appendix I.

5. Conclusion

We present strong evidence supporting the use of mixed-curvature DTs and RFs. In particular, we motivate and describe our entire algorithm and demonstrate its effectiveness across a highly diverse set of 57 benchmarks.

Product DTs and RFs offer a valuable balance of expressiveness and simplicity, positioned between extremely legible but underpowered linear classifiers and powerful but uninterpretable neural networks operating in product manifolds. We believe that these qualities, combined with their demonstrated performance across our benchmark datasets, are compelling evidence of our method’s usefulness in a non-Euclidean data analysis toolkit.

Limitations. While we view our work as downstream of signature selection and embedding generation, its value heavily depends on the availability of good product manifold embeddings. There are challenges in selecting appropriate signatures (Borde et al., 2023a), and product manifolds are not able to represent all patterns in data (Borde & Kratsios, 2023). Furthermore, it is computationally intensive to generate embeddings. There are also tradeoffs between DTs and RFs and other high-performing methods, especially graph neural networks when topologies are known. The complexity of working with non-Euclidean data could pose a potential barrier to adoption. Finally, the lack of a privileged basis (Elhage et al., 2023) in non-Euclidean embeddings makes the inductive bias of decision trees less well-motivated.

Future work. It may be possible to exploit non-privileged basis dimensions using approaches such as rotation forests (Bagnall et al., 2020), random 2-D subspace angles, or oblique decision trees. A continuous unification of all three geometries, like the κ -stereographic model described in (Skopek et al., 2020), may be more robust and elegant. Extensions to simplex geometry (Mishra et al., 2020) are also worth considering.

Impact statement

This paper presents work whose goal is to advance the field of Machine Learning. There are many potential societal consequences of our work, none of which we feel must be specifically highlighted here.

References

- 10x Genomics. Hodgkin’s Lymphoma, Dissociated Tumor: Targeted, Immunology Panel, 2020a. URL <https://www.10xgenomics.com/datasets/hodgkins-lymphoma-dissociated-tumor-targeted-immunology-panel-3-1-standard-4-0-0>.
- 10x Genomics. PBMCs from a Healthy Donor: Targeted-Compare, Immunology Panel, 2020b. URL <https://www.10xgenomics.com/datasets/pbm-cs-from-a-healthy-donor-targeted-compare-immunology-panel-3-1-standard-4-0-0>.
- Lada A. Adamic and Natalie Glance. The political blogosphere and the 2004 U.S. election: divided they blog. In *Proceedings of the 3rd international workshop on Link discovery*, LinkKDD ’05, pp. 36–43, New York, NY, USA, August 2005. Association for Computing Machinery. ISBN 978-1-59593-215-0. doi: 10.1145/1134271.1134277. URL <https://doi.org/10.1145/1134271.1134277>.
- Gregor Bachmann, Gary Bécigneul, and Octavian-Eugen Ganea. Constant Curvature Graph Convolutional Networks, May 2020. URL <http://arxiv.org/abs/1911.05076>. arXiv:1911.05076 [cs].
- A. Bagnall, M. Flynn, J. Large, J. Line, A. Bostrom, and G. Cawley. Is rotation forest the best classifier for problems with continuous features?, April 2020. URL <http://arxiv.org/abs/1809.06705>. arXiv:1809.06705 [cs].
- Gary Bécigneul and Octavian-Eugen Ganea. Riemannian Adaptive Optimization Methods. September 2018. URL <https://openreview.net/forum?id=rlei qi09K7>.
- Yoshua Bengio, Aaron Courville, and Pascal Vincent. Representation Learning: A Review and New Perspectives, April 2014. URL <http://arxiv.org/abs/1206.5538>. arXiv:1206.5538.
- Haitz Saez de Ocariz Borde, Alvaro Arroyo, Ismael Morales, Ingmar Posner, and Xiaowen Dong. Neural Latent Geometry Search: Product Manifold Inference via Gromov-Hausdorff-Informed Bayesian Optimization, October 2023a. URL <http://arxiv.org/abs/2309.04810>. arXiv:2309.04810.
- Haitz Sáez de Ocaríz Borde and Anastasis Kratsios. Neural Snowflakes: Universal Latent Graph Inference via Trainable Latent Geometries, October 2023. URL <http://arxiv.org/abs/2310.15003>. arXiv:2310.15003.
- Haitz Sáez de Ocaríz Borde, Anees Kazi, Federico Barbero, and Pietro Liò. Latent Graph Inference using Product Manifolds, June 2023b. URL <http://arxiv.org/abs/2211.16199>. arXiv:2211.16199 [cs].
- Haitz Sáez de Ocaríz Borde, Anastasis Kratsios, Marc T. Law, Xiaowen Dong, and Michael Bronstein. Neural Spacetimes for DAG Representation Learning, August 2024. URL <http://arxiv.org/abs/2408.13885>. arXiv:2408.13885.
- Leo Breiman. Random forests. *Machine Learning*, 45(1): 5–32, October 2001. ISSN 1573-0565. doi: 10.1023/A:1010933404324. URL <https://doi.org/10.1023/A:1010933404324>.
- Leo Breiman. *Classification and Regression Trees*. Routledge, New York, October 2017. ISBN 978-1-315-13947-0. doi: 10.1201/9781315139470.
- Louis Capitaine, Jérémie Bigot, Rodolphe Thiébaud, and Robin Genuer. Fréchet random forests for metric space valued regression with non euclidean predictors, February 2024. URL <http://arxiv.org/abs/1906.01741>. arXiv:1906.01741 [stat].
- Lawrence Cayton. Algorithms for manifold learning. 2005.
- Benjamin Paul Chamberlain, James Clough, and Marc Peter Deisenroth. Neural Embeddings of Graphs in Hyperbolic Space, May 2017. URL <http://arxiv.org/abs/1705.10359>. arXiv:1705.10359.
- Ines Chami, Rex Ying, Christopher Ré, and Jure Leskovec. Hyperbolic Graph Convolutional Neural Networks, October 2019. URL <http://arxiv.org/abs/1910.12933>. arXiv:1910.12933 [cs, stat].
- Philippe Chlenski, Ethan Turok, Antonio Moretti, and Itsik Pe’er. Fast hyperboloid decision tree algorithms, March 2024. URL <http://arxiv.org/abs/2310.13841>. arXiv:2310.13841 [cs].
- Sungjun Cho, Seunghyuk Cho, Sungwoo Park, Hankook Lee, Honglak Lee, and Moontae Lee. Curve Your Attention: Mixed-Curvature Transformers for Graph Representation Learning, September 2023. URL <http://arxiv.org/abs/2309.04082>. arXiv:2309.04082 [cs].
- Jiarui Ding and Aviv Regev. Deep generative model embedding of single-cell RNA-Seq profiles on hyperspheres and hyperbolic spaces. *Nature Communications*, 12(1): 2554, May 2021. ISSN 2041-1723. doi: 10.1038/s414

- 67-021-22851-4. URL <https://www.nature.com/articles/s41467-021-22851-4>. Publisher: Nature Publishing Group.
- Manfredo Do Carmo. *Riemannian Geometry*. Springer US, 1992. URL <https://link.springer.com/book/9780817634902>.
- Lars Doorenbos, Pablo Márquez-Neila, Raphael Sznitman, and Pascal Mettes. Hyperbolic Random Forests, August 2023. URL <http://arxiv.org/abs/2308.13279>. arXiv:2308.13279 [cs].
- Nelson Elhage, Robert Lasenby, and Christopher Olah. Privileged Bases in the Transformer Residual Stream, 2023. URL <https://transformer-circuits.pub/2023/privileged-basis/index.html>.
- Fedoriano. Traffic Prediction Dataset, 2020. URL <https://www.kaggle.com/datasets/fedoriano/traffic-prediction-dataset>.
- Octavian-Eugen Ganea, Gary Bécigneul, and Thomas Hofmann. Hyperbolic Neural Networks, June 2018. URL <http://arxiv.org/abs/1805.09112>. arXiv:1805.09112 [cs].
- C. Lee Giles, Kurt D. Bollacker, and Steve Lawrence. CiteSeer: an automatic citation indexing system. In *Proceedings of the third ACM conference on Digital libraries*, DL '98, pp. 89–98, New York, NY, USA, May 1998. Association for Computing Machinery. ISBN 978-0-89791-965-4. doi: 10.1145/276675.276685. URL <https://dl.acm.org/doi/10.1145/276675.276685>.
- Francesco Di Giovanni, Giulia Luise, and Michael Bronstein. Heterogeneous manifolds for curvature-aware graph embedding, February 2022. URL <http://arxiv.org/abs/2202.01185>. arXiv:2202.01185.
- M. Girvan and M. E. J. Newman. Community structure in social and biological networks. *Proceedings of the National Academy of Sciences of the United States of America*, 99(12):7821–7826, June 2002. ISSN 0027-8424. doi: 10.1073/pnas.122653799. URL <https://www.ncbi.nlm.nih.gov/pmc/articles/PMC122977/>.
- Albert Gu, Frederic Sala, Beliz Gunel, and Christopher Ré. Learning Mixed-Curvature Representations in Product Spaces. September 2018. URL <https://openreview.net/forum?id=HJxeWnCcF7>.
- Aric A. Hagberg, Daniel A. Schult, and Pieter J. Swart. Exploring Network Structure, Dynamics, and Function using NetworkX. pp. 11–15, Pasadena, California, June 2008. doi: 10.25080/TCWV9851. URL <https://doi.curvenote.com/10.25080/TCWV9851>.
- John D. Hunter. Matplotlib: A 2D Graphics Environment. *Computing in Science & Engineering*, 9(3):90–95, May 2007. ISSN 1558-366X. doi: 10.1109/MCSE.2007.55. URL <https://ieeexplore.ieee.org/document/4160265>. Conference Name: Computing in Science & Engineering.
- David S. Johnson. The genealogy of theoretical computer science: a preliminary report. *SIGACT News*, 16(2):36–49, July 1984. ISSN 0163-5700. doi: 10.1145/1008959.1008960. URL <https://dl.acm.org/doi/10.1145/1008959.1008960>.
- Allan R. Jones, Caroline C. Overly, and Susan M. Sunkin. The Allen Brain Atlas: 5 years and beyond. *Nature Reviews Neuroscience*, 10(11):821–828, November 2009. ISSN 1471-0048. doi: 10.1038/nrn2722. URL <https://www.nature.com/articles/nrn2722>. Publisher: Nature Publishing Group.
- Diederik P. Kingma and Jimmy Ba. Adam: A Method for Stochastic Optimization, January 2017. URL <http://arxiv.org/abs/1412.6980>. arXiv:1412.6980 [cs].
- Donald Ervin Knuth. *The Stanford GraphBase : a platform for combinatorial computing*. New York, N.Y. : ACM Press ; Reading, Mass. : Addison-Wesley, 1993. ISBN 978-0-201-54275-2. URL <http://archive.org/details/stanfordgraphbas00knut>.
- Max Kochurov, Rasul Karimov, and Serge Kozlukov. Geoopt: Riemannian Optimization in PyTorch, July 2020. URL <http://arxiv.org/abs/2005.02819>. arXiv:2005.02819 [cs].
- Valdis Krebs. Books about US politics, 2004. URL <http://www.orgnet.com>.
- Dmitri Krioukov, Fragkiskos Papadopoulos, Maksim Kitsak, Amin Vahdat, and Marián Boguñá. Hyperbolic geometry of complex networks. *Physical Review E*, 82(3):036106, September 2010. doi: 10.1103/PhysRevE.82.036106. URL <https://link.aps.org/doi/10.1103/PhysRevE.82.036106>. Publisher: American Physical Society.
- Alex Krizhevsky. Learning Multiple Layers of Features from Tiny Images. 2009.
- Y. Lecun, L. Bottou, Y. Bengio, and P. Haffner. Gradient-based learning applied to document recognition. *Proceedings of the IEEE*, 86(11):2278–2324, November 1998. ISSN 1558-2256. doi: 10.1109/5.726791. URL <https://ieeexplore.ieee.org/document/726791>. Conference Name: Proceedings of the IEEE.

- Adam Li, Ronan Perry, Chester Huynh, Tyler M. Tomita, Ronak Mehta, Jesus Arroyo, Jesse Patsolic, Benjamin Falk, and Joshua T. Vogelstein. Manifold Oblique Random Forests: Towards Closing the Gap on Convolutional Deep Networks, September 2022. URL <http://arxiv.org/abs/1909.11799>. arXiv:1909.11799 [cs].
- Kaibei Li, Yihao Zhang, Junlin Zhu, Xiaokang Li, and Xibin Wang. Multi-space interaction learning for disentangled knowledge-aware recommendation. *Expert Systems with Applications*, 254:124458, November 2024. ISSN 0957-4174. doi: 10.1016/j.eswa.2024.124458. URL <https://www.sciencedirect.com/science/article/pii/S0957417424013241>.
- David Lusseau, Karsten Schneider, Oliver J. Boisseau, Patti Haase, Elisabeth Slooten, and Steve M. Dawson. The bottlenose dolphin community of Doubtful Sound features a large proportion of long-lasting associations. *Behavioral Ecology and Sociobiology*, 54(4):396–405, September 2003. ISSN 1432-0762. doi: 10.1007/s00265-003-0651-y. URL <https://doi.org/10.1007/s00265-003-0651-y>.
- Daniel McNeela, Frederic Sala, and Anthony Gitter. Product Manifold Representations for Learning on Biological Pathways, January 2024. URL <http://arxiv.org/abs/2401.15478>. arXiv:2401.15478 [cs, q-bio].
- Bamdev Mishra, Hiroyuki Kasai, and Pratik Jawanpuria. Riemannian optimization on the simplex of positive definite matrices, November 2020. URL <http://arxiv.org/abs/1906.10436>. arXiv:1906.10436.
- Yoshihiro Nagano, Shoichiro Yamaguchi, Yasuhiro Fujita, and Masanori Koyama. A Wrapped Normal Distribution on Hyperbolic Space for Gradient-Based Learning, May 2019. URL <http://arxiv.org/abs/1902.02992>. arXiv:1902.02992 [cs, stat].
- M. E. J. Newman. Finding community structure in networks using the eigenvectors of matrices, May 2006. URL <https://arxiv.org/abs/physics/0605087v3>.
- Tuc Nguyen-Van, Dung D. Le, and The-Anh Ta. Improving Heterogeneous Graph Learning with Weighted Mixed-Curvature Product Manifold, July 2023. URL <http://arxiv.org/abs/2307.04514>. arXiv:2307.04514 [cs].
- Maximilian Nickel and Douwe Kiela. Poincaré Embeddings for Learning Hierarchical Representations, May 2017. URL <http://arxiv.org/abs/1705.08039>. arXiv:1705.08039.
- Fabian Pedregosa, Gaël Varoquaux, Alexandre Gramfort, Vincent Michel, Bertrand Thirion, Olivier Grisel, Mathieu Blondel, Peter Prettenhofer, Ron Weiss, Vincent Dubourg, Jake Vanderplas, Alexandre Passos, David Cournapeau, Matthieu Brucher, Matthieu Perrot, and Edouard Duchesnay. Scikit-learn: Machine Learning in Python. *Journal of Machine Learning Research*, 12(85):2825–2830, 2011. ISSN 1533-7928. URL <http://jmlr.org/papers/v12/pedregosa11a.html>.
- Prithviraj Sen, Galileo Namata, Mustafa Bilgic, Lise Getoor, Brian Gallagher, and Tina Eliassi-Rad. Collective Classification in Network Data. *AI Mag.*, 29(3):93–106, September 2008. ISSN 0738-4602. doi: 10.1609/aimag.v29i3.2157. URL <https://doi.org/10.1609/aimag.v29i3.2157>.
- Ondrej Skopek, Octavian-Eugen Ganea, and Gary Bécigneul. Mixed-curvature Variational Autoencoders, February 2020. URL <http://arxiv.org/abs/1911.08411>. arXiv:1911.08411 [cs, stat].
- Rishi Sonthalia and Anna C. Gilbert. Tree! I am no Tree! I am a Low Dimensional Hyperbolic Embedding, October 2020. URL <http://arxiv.org/abs/2005.03847>. arXiv:2005.03847 [cs, math, stat].
- Li Sun, Zhongbao Zhang, Junda Ye, Hao Peng, Jiawei Zhang, Sen Su, and Philip S. Yu. A Self-supervised Mixed-curvature Graph Neural Network, December 2021. URL <http://arxiv.org/abs/2112.05393>. arXiv:2112.05393 [cs].
- Puoya Tabaghi, Chao Pan, Eli Chien, Jianhao Peng, and Olgica Milenkovic. Linear Classifiers in Product Space Forms, February 2021. URL <http://arxiv.org/abs/2102.10204>. arXiv:2102.10204 [cs, stat] version: 1.
- Puoya Tabaghi, Michael Khanzadeh, Yusu Wang, and Sivash Mirarab. Principal Component Analysis in Space Forms, July 2024. URL <http://arxiv.org/abs/2301.02750>. arXiv:2301.02750 [cs, eess, math, stat].
- Dimosthenis Tsagkrasoulis and Giovanni Montana. Random Forest regression for manifold-valued responses, February 2017. URL <http://arxiv.org/abs/1701.08381>. arXiv:1701.08381 [stat].
- Marco Virgolin. Time complexity for different machine learning algorithms, February 2021. URL https://marcovirgolin.github.io/extras/details_time_complexity_machine_learning_algorithms/.
- Shen Wang, Xiaokai Wei, Cicero Nogueira Nogueira dos Santos, Zhiguo Wang, Ramesh Nallapati, Andrew Arnold, Bing Xiang, Philip S. Yu, and Isabel F. Cruz. Mixed-Curvature Multi-Relational Graph Neural Network for

Knowledge Graph Completion. In *Proceedings of the Web Conference 2021*, WWW '21, pp. 1761–1771, New York, NY, USA, June 2021. Association for Computing Machinery. ISBN 978-1-4503-8312-7. doi: 10.1145/3442381.3450118. URL <https://doi.org/10.1145/3442381.3450118>.

Wikipedia. List of cities by average temperature, August 2024. URL https://en.wikipedia.org/w/index.php?title=List_of_cities_by_average_temperature&oldid=1241784795#cite_note-1. Page Version ID: 1241784795.

Wayne W. Zachary. An Information Flow Model for Conflict and Fission in Small Groups. *Journal of Anthropological Research*, 33(4):452–473, 1977. ISSN 0091-7710. URL <https://www.jstor.org/stable/3629752>. Publisher: [University of New Mexico, University of Chicago Press].

Sharon Zhang, Amit Moscovich, and Amit Singer. Product Manifold Learning. In *Proceedings of The 24th International Conference on Artificial Intelligence and Statistics*, pp. 3241–3249. PMLR, March 2021. URL <https://proceedings.mlr.press/v130/zhang21j.html>. ISSN: 2640-3498.

Grace X. Y. Zheng, Jessica M. Terry, Phillip Belgrader, Paul Ryvkin, Zachary W. Bent, Ryan Wilson, Solongo B. Ziraldo, Tobias D. Wheeler, Geoff P. McDermott, Junjie Zhu, Mark T. Gregory, Joe Shuga, Luz Montesclaros, Jason G. Underwood, Donald A. Masquelier, Stefanie Y. Nishimura, Michael Schnall-Levin, Paul W. Wyatt, Christopher M. Hindson, Rajiv Bharadwaj, Alexander Wong, Kevin D. Ness, Lan W. Beppu, H. Joachim Deeg, Christopher McFarland, Keith R. Loeb, William J. Valente, Nolan G. Ericson, Emily A. Stevens, Jerald P. Radich, Tarjei S. Mikkelsen, Benjamin J. Hindson, and Jason H. Bielas. Massively parallel digital transcriptional profiling of single cells. *Nature Communications*, 8(1):14049, January 2017. ISSN 2041-1723. doi: 10.1038/ncomms14049. URL <https://www.nature.com/articles/ncomms14049>. Publisher: Nature Publishing Group.

A. Gaussian mixture details

A.1. Overall structure

The structure of our sampling algorithm is as follows. Note that, rather than letting \mathcal{M} be a manifold of arbitrary curvature, we force its curvature to be one of $\{-1, 0, 1\}$ for implementation reasons. This necessitates rescaling steps, which take place in Equations 29, 33, and 39. The result is equivalent to performing the equivalent steps, without rescaling, on a manifold of the proper curvature.

1. Generate \mathbf{c} , a vector that divides m samples into n clusters:

$$\mathbf{p}_{\text{raw}} = \langle p_0, p_1, \dots, p_{n-1} \rangle \quad (23)$$

$$p_i \sim \text{Uniform}(0, 1) \quad (24)$$

$$\mathbf{p}_{\text{norm}} = \frac{\mathbf{p}_{\text{raw}}}{\sum_{i=0}^{n-1} p_i} \quad (25)$$

$$\mathbf{c} = \langle c_0, c_1, \dots, c_{m-1} \rangle \quad (26)$$

$$c_i \sim \text{Categorical}(n, \mathbf{p}_{\text{norm}}) \quad (27)$$

2. Sample \mathbf{M}_{euc} , an $n \times D$ matrix of n class means:

$$\mathbf{M}_{\text{euc}} = \langle \mathbf{m}_0, \mathbf{m}_1, \dots, \mathbf{m}_{n-1} \rangle^T \quad (28)$$

$$\mathbf{m}_i \sim \mathcal{N}(0, \sqrt{K}\mathbf{I}). \quad (29)$$

3. Move \mathbf{M}_{euc} into $T_0\mathcal{M}$, the tangent plane at the origin of \mathcal{M} , by applying $\psi : \mathbf{x} \rightarrow \langle 0, \mathbf{x} \rangle$ per-row to \mathbf{M}_{euc} :

$$\mathbf{M}_{\text{tan}} = \langle \psi(\mathbf{m}_0), \psi(\mathbf{m}_1), \dots, \psi(\mathbf{m}_{n-1}) \rangle^T, \quad (30)$$

$$\psi : \mathbb{R}^D \rightarrow \mathbb{R}^{D+1}, \mathbf{x} \rightarrow \langle 0, \mathbf{x} \rangle. \quad (31)$$

4. Project \mathbf{M}_{tan} onto \mathcal{M} using the exponential map from $T_0\mathcal{M}$ to \mathbf{M}_{tan} :

$$\mathbf{M} = \exp_0(\mathbf{M}_{\text{tan}}). \quad (32)$$

5. For $0 \leq i < n$, sample a corresponding covariance matrix. Here, σ is a variance scale parameter that can be set:

$$\Sigma_i \sim \text{Wishart}(\sigma\sqrt{K}\mathbf{I}, D) \quad (33)$$

6. For $0 \leq j < m$, sample \mathbf{X}_{euc} , a matrix of m points according to their clusters' covariance matrices:

$$\mathbf{X}_{\text{euc}} = \langle \mathbf{x}_0, \mathbf{x}_1, \dots, \mathbf{x}_{m-1} \rangle^T \quad (34)$$

$$x_j \sim \mathcal{N}(0, \Sigma_{\mathbf{c}_j}). \quad (35)$$

7. Apply $\psi(\cdot)$ from Eq 31 to each \mathbf{x}_j to move it into $T_0\mathcal{M}$:

$$\mathbf{X}_{\text{tan}} = \langle \psi(\mathbf{x}_0), \psi(\mathbf{x}_1), \dots, \psi(\mathbf{x}_{m-1}) \rangle^T. \quad (36)$$

8. For each row in \mathbf{X}_{tan} , apply parallel transport from $T_0\mathcal{M}$ to its class mean:

$$\mathbf{X}_{\text{PT}} = \langle \mathbf{x}_{0,\mu}, \mathbf{x}_{1,\mu}, \dots, \mathbf{x}_{m-1,\mu} \rangle \quad (37)$$

$$\mathbf{x}_{j,\mu} = PT_{0 \rightarrow \mathbf{m}_{\mathbf{c}_j}}(\mathbf{x}_j) \quad (38)$$

9. Use the exponential map at $T_\mu\mathcal{M}$ to move the points onto the manifold:

$$\mathbf{X}_{\mathcal{M}} = \langle \mathbf{x}_{0,\mathcal{M}}, \mathbf{x}_{1,\mathcal{M}}, \dots, \mathbf{x}_{m-1,\mathcal{M}} \rangle \quad (39)$$

$$\mathbf{x}_{j,\mathcal{M}} = \frac{\exp_{\mathbf{m}_{\mathbf{c}_j}}(\mathbf{x}_{j,\mu})}{\sqrt{K}} \quad (40)$$

10. Repeat steps 2–9 for as many manifolds as desired; produce a final embedding by concatenating all component embeddings column-wise:

$$\mathbf{X} = \langle \mathbf{X}_{\mathcal{M}_0}, \mathbf{X}_{\mathcal{M}_1}, \dots, \mathbf{X}_{\mathcal{M}_p} \rangle \quad (41)$$

A.2. Equations for manifold operations

First, we provide the forms of the parallel transport operation in hyperbolic, hyperspherical, and Euclidean spaces:

$$\text{PT}_{\nu \rightarrow \mu}^{\mathbb{H}}(\mathbf{v}) = \mathbf{v} + \frac{\langle \mu - \alpha\nu, \nu \rangle_{\mathcal{L}}}{\alpha + 1}(\nu + \mu) \quad (42)$$

$$\alpha = -\langle \nu, \mu \rangle_{\mathcal{L}} \quad (43)$$

$$\text{PT}_{\nu \rightarrow \mu}^{\mathbb{S}}(\mathbf{v}) = \mathbf{v} \cos(d) + \frac{\sin(d)}{d}(\mu - \cos(d)\nu) \quad (44)$$

$$d = \cos^{-1}(\nu \cdot \mu) \quad (45)$$

$$\text{PT}_{\nu \rightarrow \mu}^{\mathbb{E}}(\mathbf{v}) = \mathbf{v} + \mu - \nu. \quad (46)$$

The exponential map is defined as follows in each of the three spaces:

$$\exp_{\mu}^{\mathbb{H}}(\mathbf{u}) = \cosh(\|\mathbf{u}\|_{\mathcal{L}})\mu + \sinh(\|\mathbf{u}\|_{\mathcal{L}}) \frac{\mathbf{u}}{\|\mathbf{u}\|_{\mathcal{L}}} \quad (47)$$

$$\exp_{\mu}^{\mathbb{S}}(\mathbf{u}) = \cos(\|\mathbf{u}\|)\mu + \sin(\|\mathbf{u}\|) \frac{\mathbf{u}}{\|\mathbf{u}\|} \quad (48)$$

$$\exp_{\mu}^{\mathbb{E}}(\mathbf{u}) = \mathbf{u}. \quad (49)$$

A.3. Generating classification targets

To generate classification targets covering $p \leq n$ classes, all we need to do is map clusters to classes. To ensure that each class has at least one associated cluster, we arbitrarily assign the first p clusters to the first p classes. In the $p = n$ case, this is equal to the p -dimensional identity matrix, and we conclude. In the $p < n$ case, we assign the remaining $n - p$ by drawing assignments from a uniform categorical distribution over the p classes.

A.4. Generating regression targets

To generate regression targets, we draw per-cluster slopes and intercepts:

$$\beta_{i,k} \sim \text{Uniform}(-1, 1) \quad (50)$$

$$\alpha_i \sim \text{Uniform}(-10, 10) \quad (51)$$

We then multiply each $x_j \in \mathbf{X}_{\text{euc}}$ (i.e. the pre-transport samples from the normal distribution) by β and add α :

$$y_j = \mathbf{x}_j \beta + \alpha + \varepsilon \quad (52)$$

To make the regression task more constrained and, therefore, to make the RMSEs across samples more comparable, we further normalize the labels to the range $[0, 1]$ by subtracting the minimum y value and dividing by the range.

A.5. Relationship to other work

Nagano et al. (2019) developed the overall technique used for a single cluster and a single manifold, i.e. steps 6–9. Chlenski et al. (2024) modified this method to work for mixtures of Gaussians in $\mathbb{H}^{d,1}$, and deployed it for $d \in 2, 4, 8, 16$. This corresponds to steps 1–5 of our procedure (although note that our covariance matrices are sampled differently in step 5). Thus, our contribution is simply to add step 10, modify step 5 to use the Wishart distribution, to add curvature-related scaling factors in Equations 29, 33, and 39, and to generate classification and regression targets as described in the preceding sections.

We apply this to *hyperspherical* manifolds, for which the von Mises-Fisher (VMF) distribution is typically preferred. This is an unconventional choice, but has been employed previously by Skopek et al. (2020) in their mixed-curvature VAE formulation. We do not argue for the superiority of our approach over the VMF distribution in general; however, we prefer to use ours for these benchmarks, as it allows us to draw simpler parallels between manifolds of different curvatures.

B. Product space decision tree pseudocode

Algorithm 1 Product Space Decision Tree

```

1: Procedure FIT:
2:    $\mathcal{P}$     (signature of) product manifold
3:    $\mathbf{X}$     data points
4:    $\mathbf{y}$     target labels
5: Initialize:
6:    $\mathcal{T}$     an empty tree
7: return FITTREE( $\mathbf{X}, \mathbf{y}, 0$ )
8:
9: Procedure FITTREE:
10:   $\mathbf{X}$     data points
11:   $\mathbf{y}$     target labels
12:   $t$     current depth of the tree.
13: Initialize:
14:   $d_{\text{best}}$  dimension of best split,
15:   $\theta_{\text{best}}$  angle of best split,
16:   $IG_{\text{best}}$  information gain of best split.
17: for each  $d \in \mathbf{D}'$  do
18:    $\mathcal{M} \leftarrow$  component manifold for dimension  $d$ 
19:    $\Theta \leftarrow$  GETCANDIDATES( $\mathcal{M}, \mathbf{X}, d$ )
20:   for each candidate  $\theta \in \Theta$  do
21:    Partition  $\mathbf{X}, \mathbf{y}$  into  $\mathbf{X}^+, \mathbf{X}^-, \mathbf{y}^+, \mathbf{y}^-$  via Eq. 16.
22:    Apply Eq. 13 on  $\mathbf{y}^+, \mathbf{y}^-$  to compute  $IG_{\text{current}}$ 
23:    if  $IG_{\text{current}} > IG_{\text{best}}$  then
24:      $d_{\text{best}}, \theta_{\text{best}}, IG_{\text{best}} \leftarrow d, \theta, IG_{\text{current}}$ 
25:    end if
26:   end for
27: end for
28: if no valid split was found then
29:   return  $\mathcal{N}$ , a new leaf node with  $\mathbf{y}$  probabilities.
30: else
31:   Create  $\mathcal{N}$ , a decision node with  $d_{\text{best}}$  and  $\theta_{\text{best}}$ 
32:    $\mathcal{N}_L \leftarrow$  FITTREE( $\mathbf{X}^-, \mathbf{y}^-, t + 1$ )
33:    $\mathcal{N}_R \leftarrow$  FITTREE( $\mathbf{X}^+, \mathbf{y}^+, t + 1$ )
34:   return  $\mathcal{N}$  with left child  $\mathcal{N}_L$  and right child  $\mathcal{N}_R$ 
35: end if
36:
37: Procedure GETCANDIDATES:
38:   $\mathcal{M}$     A component manifold
39:   $\mathbf{X}$     A dataset of points in  $\mathcal{M}$ 
40:   $d$     A dimension index
41: if  $d$  is the special dimension then
42:   return empty array []
43: end if
44:  $\Theta \leftarrow$  Angles of  $\mathbf{X}$  via Eq. 15
45:  $\Theta \leftarrow$  sort and deduplicate  $\Theta$ 
46: return [ $\theta_m$  for  $\theta_i, \theta_{i+1} \in \Theta$  via Eq. 18, 20, or 22] (depending on curvature of  $\mathcal{M}$ ).
    
```

C. Proof of equivalence for Euclidean case

A classical CART tree splits data points according to whether their value in a given dimension is greater than or less than some threshold value t . Midpoints are simple arithmetic means. This can be written as:

$$S'(\mathbf{x}, d, t) = \begin{cases} 1 & \text{if } x_d > t, \\ 0 & \text{otherwise.} \end{cases} \quad (53)$$

$$m_{DT}(\mathbf{u}, \mathbf{v}) = \frac{u_d + v_d}{2}. \quad (54)$$

In our transformed DT, we lift the data points by applying $\phi : \mathbf{x} \rightarrow (1, \mathbf{x})$ and then check which side of an axis-inclined hyperplane they fall on. The splitting function is based on the angle θ of inclination with respect to the $(0, d)$ plane, i.e., $\langle 1, x_d \rangle$. Our midpoints are computed to ensure equidistance in the original manifold:

$$S(\mathbf{x}, d, \theta) = \text{sign}(\sin(\theta)x_d - \cos(\theta)x_0) \quad (55)$$

$$m_{\mathbb{E}}(\mathbf{u}, \mathbf{v}) = \tan^{-1} \left(\frac{2}{u_d + v_d} \right) \quad (56)$$

To demonstrate the equivalence of the classical DT formulation to our transformed algorithm in \mathbb{E} , we will show that Equation 53 is equivalent to Equation 55 and Equation 54 is equivalent to Equation 56 under

$$\theta = \cot^{-1}(t). \quad (57)$$

C.1. Equivalence of Splits

First, we show that Equations 53 and 55 are equivalent, assuming $t \neq 0$:

$$S(\mathbf{x}, d, \theta) = \text{sign}(\sin(\theta)x_d - \cos(\theta)x_0) = 1 \quad (58)$$

$$\iff \sin(\theta)x_d - \cos(\theta) > 0 \quad (59)$$

$$\iff \frac{\sin(\theta)}{\cos(\theta)}x_d = \tan(\theta)x_d > 1 \quad (60)$$

$$\iff x_d/t > 1 \quad (61)$$

$$\iff x_d > t \quad (62)$$

$$\iff S'(\mathbf{x}, d, t) = 1 \quad (63)$$

C.2. Equivalence of midpoints

Now, we show that Equations 54 and 56 are equivalent:

$$\cot^{-1}(m_{DT}(\mathbf{u}, \mathbf{v})) = \cot^{-1} \left(\frac{u_d + v_d}{2} \right) \quad (64)$$

$$= \tan^{-1} \left(\frac{2}{u_d + v_d} \right) \quad (65)$$

$$= m_{\mathbb{E}}(\mathbf{u}, \mathbf{v}) \quad (66)$$

D. Summary of angular midpoint formulas

Table 5: Distance functions and midpoint angle formulas for each component manifold type.

Manifold \mathcal{M}	Distance $\delta_{\mathcal{M}}(\mathbf{u}, \mathbf{v})$	Midpoint angle $\theta_{\mathcal{M}}(\mathbf{u}, \mathbf{v})$
$\mathbb{S}^{D,K}$	$\cos^{-1}\left(\frac{K^2\langle\mathbf{u}, \mathbf{v}\rangle}{K}\right)$	$\frac{\theta_{\mathbf{u}} + \theta_{\mathbf{v}}}{2}$
$\mathbb{E}^{D,0}$	$\sqrt{\langle\mathbf{u}, \mathbf{v}\rangle}$	$\tan^{-1}\left(\frac{2}{u_d + v_d}\right)$
$\mathbb{H}^{D,K}$	$\frac{-\cosh^{-1}(K^2\langle\mathbf{u}, \mathbf{v}\rangle_{\mathcal{L}})}{K}$	$\cot^{-1}(V - \sqrt{V^2 - 1})$ if $\theta_{\mathbf{u}} + \theta_{\mathbf{v}} < \pi$, $\cot^{-1}(V + \sqrt{V^2 - 1})$ otherwise. $V := \frac{\sin(2\theta_{\mathbf{u}} - 2\theta_{\mathbf{v}})}{2\sin(\theta_{\mathbf{u}} + \theta_{\mathbf{v}})\sin(\theta_{\mathbf{v}} - \theta_{\mathbf{u}})}$

E. Full benchmark details

E.1. Product DT/RF hyperparameters

For our models, we set the `n_features = "n_choose_2"` parameter. This means that we consider all $\binom{n}{2}$ linear projections. We do this because we restrict ourselves to 2-dimensional component manifolds, and therefore we only observe $\binom{3}{2} = 3$ total angles, equal to the number of features used by ambient space Euclidean methods. All other hyperparameters are set identically to the scikit-learn DT/RF settings below.

E.2. Scikit-learn hyperparameters

Random forests and decision trees. For fairness, we set all DT and RF hyperparameters identically. Specifically, we set the following hyperparameters for both DTs and RFs:

- `max_depth = 5`
- `min_samples_split = 2`
- `min_samples_leaf = 1`
- `min_impurity_decrease = 0.0`

For RFs, we also set the following hyperparameters:

- `n_estimators = 12`
- `max_features = "sqrt"`
- `bootstrap = True` (subsamples the training data)
- `max_samples = None` (draws n samples from a set of n points)

Because the scikit-learn implementation differs substantially from ours, subsamples vary even when the random seed is set. Nevertheless, we also employ the same random seed for all RF models.

k -nearest neighbor models. For k -nearest neighbors, we use default hyperparameters.

Product space perceptrons and SVMs. Product space perceptrons only have one hyperparameter, which is the relative weight assigned to each component manifold. We elect to give each component manifold equal weight.

Neither the SVM code provided by [Tabaghi et al. \(2021\)](#) nor our own reimplementations would run on our datasets. In particular, we had issues satisfying the convexity constraints described in their paper, causing the solve to crash. Correcting this mistake and augmenting our benchmarks with SVM evaluations is a direction for future research.

E.3. Neural networks

κ -GCN overview. Neural networks, especially graph neural networks, are a popular choice for representing and working with mixed-curvature representations (Sun et al., 2021; Cho et al., 2023; Bachmann et al., 2020; McNeela et al., 2024). In particular, we implement a version of the κ -GCN model described in Bachmann et al. (2020) to serve as the basis for our neural network models. This model is heavily inspired by prior work on generalizing graph convolutional networks (GCNs) in hyperbolic spaces (Chami et al., 2019; Ganea et al., 2018). Since the κ -GCN model uses different models of non-Euclidean space (the Poincaré disk for hyperbolic space and the projected sphere for hyperspherical space), we transform our points to these spaces using the standard stereographic projection:

$$\phi(\langle x_0, x_1, \dots, x_D \rangle) \rightarrow \left\langle \frac{x_1}{1 + \sqrt{|K|x_0}}, \frac{x_2}{1 + \sqrt{|K|x_0}}, \dots, \frac{x_D}{1 + \sqrt{|K|x_0}} \right\rangle. \quad (67)$$

At each layer, the κ -GCN applies a weight matrix \mathbf{W} and aggregates updated embeddings using an adjacency matrix \mathbf{A} (analogous to the traditional GCN update operation, $\mathbf{H}^{(l+1)} = \sigma(\mathbf{A}\mathbf{H}^l\mathbf{W})$), except using manifold-appropriate variants of left- and right-matrix multiplication, and applying the nonlinearity through logarithmic and exponential maps. At the final layer, the κ -GCN computes stereographic logits:

$$\mathbb{P}(y = k | \mathbf{x}) = \text{Softmax}(\text{logits}_{\mathcal{M}}(\mathbf{x}, k)) \quad (68)$$

$$\text{logits}_{\mathcal{M}}(\mathbf{x}, k) = \frac{\|\mathbf{a}_k\|_{\mathbf{p}_k}}{\sqrt{K}} \sin_K^{-1} \left(\frac{2\sqrt{|K|}\langle \mathbf{z}_k, \mathbf{a}_k \rangle}{(1 + K\|\mathbf{z}_k\|^2)\|\mathbf{a}_k\|} \right), \quad (69)$$

where \mathbf{a}_k is a column vector of the final weight matrix corresponding to class k , $\mathbf{p}_k \in \mathcal{M}$ is a bias term, and $\mathbf{z}_k = -\mathbf{p}_k \oplus \mathbf{x}$, with \oplus denoting the Möbius addition operation. It is not totally apparent in Bachmann et al. (2020) how the logits aggregate across different product manifolds; we follow Cho et al. (2023) in aggregating logits as the ℓ_2 -norm of component manifold logits, multiplied by the sign of the sum of the component inner products:

$$\text{logits}_{\mathcal{P}}(\mathbf{x}, k) = \sqrt{\sum_{\mathcal{M} \in \mathcal{P}} \text{logits}_{\mathcal{M}}(\mathbf{x}_{\mathcal{M}}, k)} \cdot \sum_{\mathcal{M} \in \mathcal{P}} \langle \mathbf{x}_{\mathcal{M}}, \mathbf{a}_{k\mathcal{M}} \rangle \quad (70)$$

Intuitively, this generalizes the notion that output logits correspond to signed distances from some hyperplane specified by the column vectors and biases of the final layer; all modifications to the standard logit formula simply reflect the behavior of distances in these manifolds.

Implementation and variants. We use our own implementation of the κ -GCN architecture, loosely based on the implementation of stereographic logits given in Cho et al. (2023). The κ -GCN class can be manipulated in several ways: in the $K = 0$ case, it behaves exactly like a Euclidean graph convolutional network; when $\mathbf{A} = \mathbf{I}$, i.e. the adjacency matrix provided is trivial, it behaves like a manifold-appropriate version of an MLP. We use this to derive the neural models we benchmark as follows:

Table 6: A summary of the neural models benchmarked in our work. Here, $\mathcal{M}_{\text{stereo}}$ denotes the stereographic projection of \mathcal{M} , D means the ambient dimension of \mathcal{M} , and $\phi(\cdot)$ is the stereographic projection.

Model	Preprocessing	Manifold	Hidden dimensions	\mathbf{A}
Ambient MLP	—	\mathbb{E}^D	$(\mathbb{E}^{32}, \mathbb{E}^{32})$	\mathbf{I}
Tangent MLP	$\log_{\mu_0}(\mathbf{X})$	\mathbb{E}^D	$(\mathbb{E}^{32}, \mathbb{E}^{32})$	\mathbf{I}
Ambient GCN	—	\mathbb{E}^D	$(\mathbb{E}^{32}, \mathbb{E}^{32})$	\mathbf{A}
Tangent GCN	$\log_{\mu_0}(\mathbf{X})$	\mathbb{E}^D	$(\mathbb{E}^{32}, \mathbb{E}^{32})$	\mathbf{A}
κ -GCN	$\phi(\mathbf{X})$	$\mathcal{M}_{\text{stereo}}$	$(\mathcal{M}_{\text{stereo}})$	\mathbf{A}
κ -MLR	$\phi(\mathbf{X})$	$\mathcal{M}_{\text{stereo}}$	$()$	\mathbf{I}

Generating adjacency matrices. For κ -GCN to work correctly, it is important that the adjacency matrix be correctly normalized. We use a standard method, as described in Bachmann et al. (2020), to generate appropriate adjacency matrices.

For some adjacency matrix \mathbf{A} , we do:

$$\mathbf{A}' = \mathbf{A} + \mathbf{A}^T \quad (71)$$

$$\tilde{\mathbf{A}} = \mathbf{A}' + \mathbf{I} \quad (72)$$

$$\tilde{D}_{ii} = \sum_k \tilde{A}_{ik} \quad (73)$$

$$\hat{\mathbf{A}} = \tilde{\mathbf{D}}^{-1/2} \tilde{\mathbf{A}} \tilde{\mathbf{D}}^{-1/2}, \quad (74)$$

i.e. \mathbf{A}' is \mathbf{A} made symmetric, $\tilde{\mathbf{A}}$ has self-connections, \mathbf{D} is a diagonal matrix of row-wise degree sums, and $\hat{\mathbf{A}}$ is the properly normalized version of \mathbf{A} .

When an adjacency matrix is not provided (i.e., for all benchmarks except the graph embeddings), we compute \mathbf{A} via a standard Gaussian kernel on the normalized pairwise distances between points:

$$A_{i,j} = \exp\left(\frac{-\delta_{\mathcal{M}}(\mathbf{x}_i, \mathbf{x}_j)}{\max_{k,l} \delta(\mathbf{x}_k, \mathbf{x}_l)}\right), \quad (75)$$

followed by the transformation from \mathbf{A} to $\hat{\mathbf{A}}$ as described above.

Classification. The stereographic logits described above can be turned into classification targets through a standard softmax function.

Regression. For regression problems, we set the output dimension of our κ -GCN to 1 and skip the final softmax. We use a mean squared error loss function to train. This variant of κ -GCN recapitulates the typical relationship between regression and classification; however, it has not previously been described. In our experience, it unfortunately tends to grossly underperform other models.

Link prediction. The link prediction variant of the κ -GCN was also not described in Bachmann et al. (2020). We follow a closely related paper, Chami et al. (2019), in the standard choice of applying the Fermi-Dirac decoder (Krioukov et al., 2010; Nickel & Kiela, 2017) to predict edges:

$$\mathbb{P}((i, j) \in \mathcal{E} | \mathbf{x}_i, \mathbf{x}_j) = \left(\exp\left(\frac{\delta_{\mathcal{M}}(\mathbf{x}_i, \mathbf{x}_j)^2 - r}{t}\right) \right), \quad (76)$$

where the embeddings for points i and j , \mathbf{x}_i and \mathbf{x}_j , may be updated by κ -GCN layers.

Shared hyperparameters. For all neural networks, we used a learning rate of .0001 and trained for 4,000 epochs. For Euclidean parameters, we used Adam (Kingma & Ba, 2017), whereas for non-Euclidean parameters we used Riemannian Adam (Becigneul & Ganea, 2018) implemented in Geopt (Kochurov et al., 2020). Both optimizers use the hyperparameters $\beta_1 = 0.9$ and $\beta_2 = 0.999$. These hyperparameters were chosen on the basis of their convergence and good performance in exploratory hyperparameter sweeps.

E.4. Graph embeddings

Learning embeddings. We reimplement the method in Gu et al. (2018) to learn graph embeddings. In particular, we use the NetworkX package (Hagberg et al., 2008) to load the graph, extract the largest connected component, and compute pairwise distances between nodes using the Floyd-Warshall algorithm. For embedding purposes, we treat all graphs as undirected. Pairwise distances were normalized into the range $[0, 1]$ by dividing by the maximum distance. To prevent train-test leakage, we take a non-transductive learning approach and mask out the gradients from the test nodes to the training nodes during the embedding process.

Embedding hyperparameters. Embeddings were learned using Riemannian Adam (Becigneul & Ganea, 2018) implemented in Geopt (Kochurov et al., 2020). For each signature, we train 10 randomly-initialized embeddings for 10,000 epochs each. We treat the first 2,000 epochs as a burn-in period, during which the learning rate is .001 and the curvature of each manifold is fixed. For the remaining epochs, we train embedding coordinates with a learning rate of 0.01 and scale factors with a learning rate of 0.001. These hyperparameters were chosen based on their stability and convergence in exploratory experiments.

Train-test split. We avoid train-test leakage during embeddings generation by masking the gradients from the test set to the training set. Similarly, we performed the train-test split at the node level for all tasks including link prediction, meaning there was not leakage through the adjacency matrix.

Evaluations. Since it was not clear *a priori* which signature would embed each graph the best, we learned 10 embeddings for each candidate signature and took the one with the best D_{avg} to be the benchmark signature. Our reasoning is that the lowest-distortion embedding of the graph is the most appropriate benchmark for evaluating the geometrical appropriateness of a classifier.

Link prediction. To generate link prediction datasets, we trained 100 randomly initialized sets of node embeddings in $\mathbb{S}^2 \times \mathbb{E}^2 \times \mathbb{H}^2$. If we let \mathbf{X} be our original node embeddings and \mathcal{E} be the ground-truth edges of the graph, we then generated the following dataset:

$$\mathbf{X}_{LP} = \{(\mathbf{x}_i, \mathbf{x}_j) \text{ for } (\mathbf{x}_i, \mathbf{x}_j, \delta_{\mathcal{P}}(\mathbf{x}_i, \mathbf{x}_j)) \in \mathbf{X}\} \quad (77)$$

$$\mathbf{y}_{LP} = \{\mathbb{I}\{(\mathbf{x}_i, \mathbf{x}_j) \in \mathcal{E}\} \text{ for } (\mathbf{x}_i, \mathbf{x}_j) \in \mathbf{X}\} \quad (78)$$

The corresponding signature is $(\mathcal{P})^2 \times \mathbb{E}^1$; in the case of our embeddings, that is $(\mathbb{S}^2 \times \mathbb{E}^2 \times \mathbb{H}^2)^2 \times \mathbb{E}^1$. For GCN-based models which use an adjacency matrix, we applied a Gaussian kernel to the normalized pairwise distances as described in Equation 75; this prevents the labels from leaking into the training process through the adjacency matrix.

E.5. VAE training

Encoder/decoder architectures. Following Tabaghi et al. (2021), we use the following encoder/decoder architectures:

- Lymphoma dataset: Two 200-dimensional hidden layers, 500 epochs
- Blood cell dataset: Three 400-dimensional hidden layers, 200 epochs
- Omniglot and MNIST: 400-dimensional latent
- CIFAR-100: 4×4 convolutional kernels with stride 2 and padding 1. Encoder: 3 CNN layers of 64, 128, and 512 channels. Decoder: 2048-dimensional dense layer, followed by 2 CNN layers of 256, 64, and 3 channels.

Training hyperparameters. Our VAEs were trained using the Adam optimizer (Kingma & Ba, 2017) with default parameters (learning rate .001, $\beta_1 = 0.9$, $\beta_2 = 0.999$). In all models, each layer except the last is followed by a ReLU activation function. Curvatures were trained identically, except using a learning rate of .0001, after 100 burn-in epochs. Because some training details were omitted from the original papers, we additionally chose the following hyperparameters:

- Batch size: 4,096
- Number of samples per point: 64
- β (weight for KL-divergence in VAE loss): 1

Train-test split. To minimize the risk of data leakage, we trained our VAEs on only the training data, then used the trained VAEs to generate embeddings for the training and test data. Embeddings were generated by running points through the VAE encoder and taking the returned mean parameter.

Evaluations. To conserve memory, we randomly subsampled 1,000 points from the training and test sets for each evaluation. We ran 10 trials per dataset in total.

E.6. Empirical datasets

Landmasses. We generated a geospatial classification dataset for land versus water prediction by sampling 1,000 points from an evenly sampled grid of 10,000 longitudes and latitudes, transforming them to 3-dimensional coordinates, and assigning a “land” or “water” label to each point using the Basemap library in Matplotlib (Hunter, 2007). For classification, we associate the 3-dimensional coordinates with the signature \mathbb{S}^2 .

Neural spiking prediction. We use patch-clamp electrophysiology datasets downloaded from the Allen Mouse Brain Atlas (Jones et al., 2009). We arbitrarily pick Neurons 33 and 46 for their nontrivial spiking dynamics. To represent signals in product spaces, we apply a Fast Fourier Transform and take the top 5 Fourier coefficients by magnitude. We then take their corresponding frequencies f_i and represent each time point in \mathbb{S}^1 via the following transformation:

$$\phi : \mathbb{R}^1 \rightarrow (\mathbb{S}^1)^5, \phi(t) = \left(\cos\left(2\pi \frac{t}{f_i}\right), \sin\left(2\pi \frac{t}{f_i}\right) \right) \Big|_{i=1}^5 \quad (79)$$

This yields a product space representation in $(\mathbb{S}^1)^5$. We plot both signals, along with their reconstruction using their top 5 Fourier components, in Figure 6.

Global temperature by month. We downloaded a list of global average monthly temperatures for the 400 largest cities in the world from Wikipedia (Wikipedia, 2024). We transform longitude and latitude into 3-D coordinates to represent our data in \mathbb{S}^2 . To convert months to \mathbb{S}^1 valued coordinates, we transform ordinal representations of months $t \in [0, 11]$ via the following transformation:

$$\phi : \mathbb{R}^1 \rightarrow \mathbb{S}^1, \phi(t) = \left(\cos \left(2\pi \frac{t}{12} \right), \sin \left(2\pi \frac{t}{12} \right) \right) \quad (80)$$

This yields a product space representation of the data in $\mathbb{S}^2 \times \mathbb{S}^1$.

Traffic prediction. We download an automobile traffic prediction dataset from Kaggle (Fedesoriano, 2020). This dataset aggregates readings across four sensors with date and time annotations. We process the date and time annotation into day of year (d), day of week (w), hour (h), and minute (m) labels and transform to $(\mathbb{S}^1)^4$ analogously to the month timestamps in the global temperature data. Letting l be the (numeric) label of the sensor, we apply the following transformation to our data:

$$\begin{aligned} \phi : \mathbb{R}^5 &\rightarrow (\mathbb{S}^1)^5 \times \mathbb{E}^1 & (81) \\ \phi(d, w, h, m, l) &= \left(\cos \left(2\pi \frac{d}{365} \right), \sin \left(2\pi \frac{d}{365} \right), \right. \\ &\quad \cos \left(2\pi \frac{w}{7} \right), \sin \left(2\pi \frac{w}{7} \right), \\ &\quad \cos \left(2\pi \frac{h}{24} \right), \sin \left(2\pi \frac{h}{24} \right), \\ &\quad \left. \cos \left(2\pi \frac{m}{60} \right), \sin \left(2\pi \frac{m}{60} \right), l \right) & (82) \end{aligned}$$

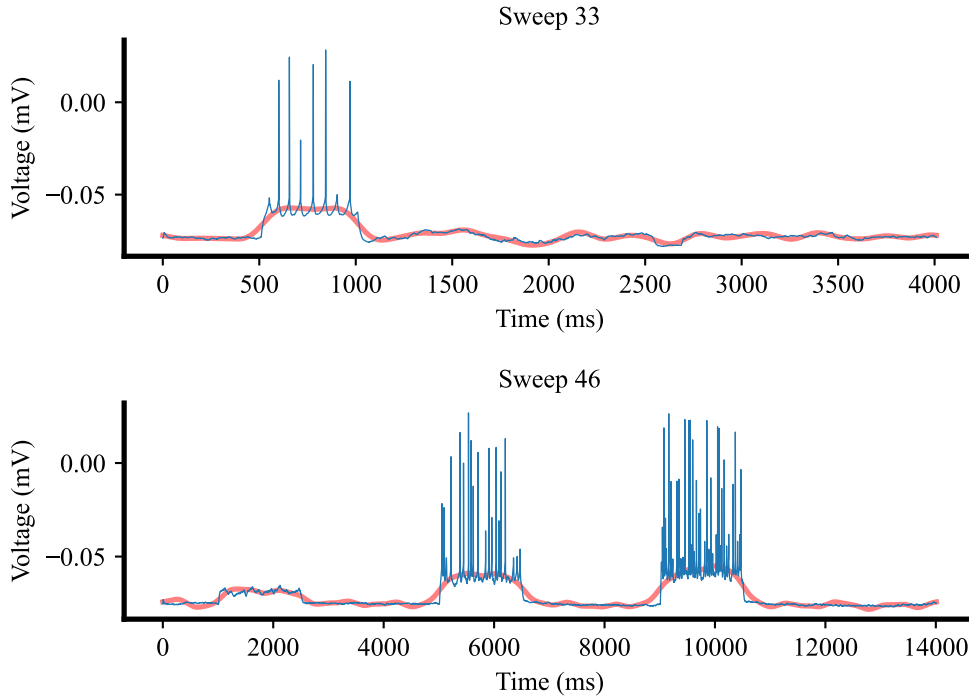
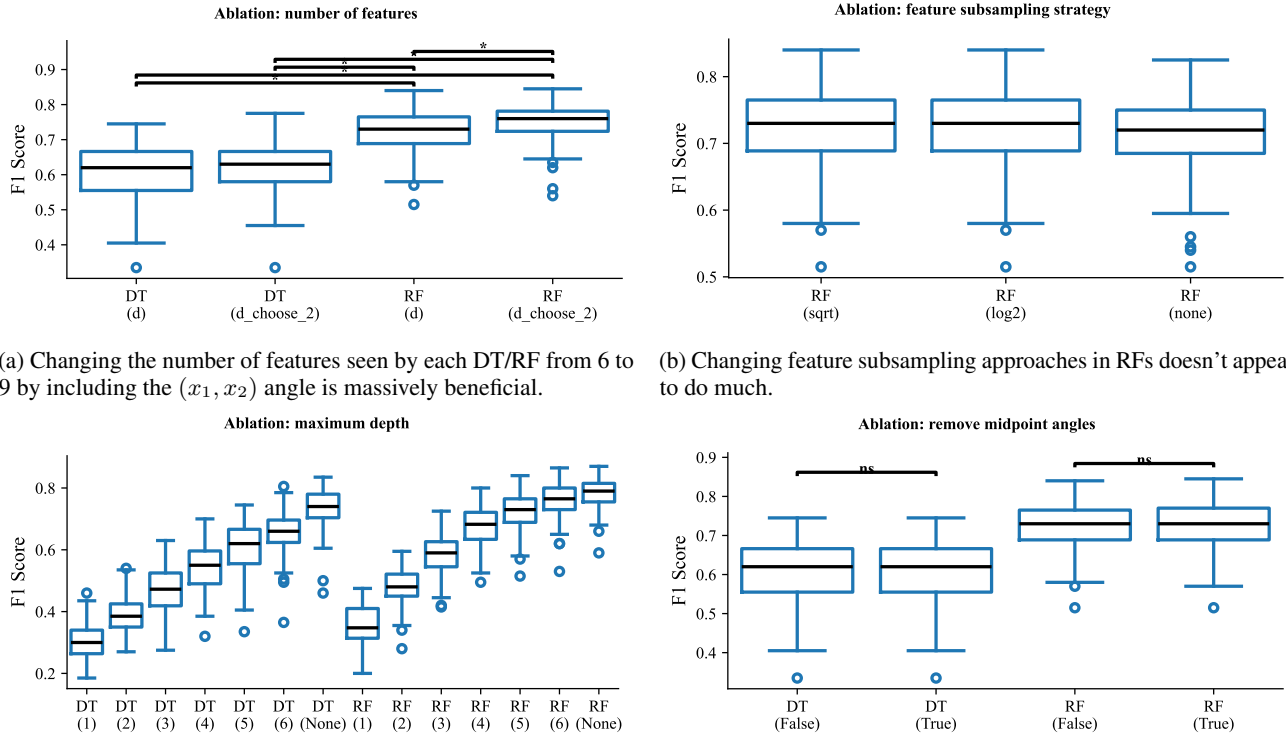


Figure 6: The “Neuron 33” and “Neuron 46” datasets, along with their reconstruction using the top 5 Fourier coefficients shown in red.

F. Ablations and effects of hyperparameters

For all experiments, we sampled 100 mixtures of 32 Gaussians using the signature $\mathcal{P} = \mathbb{S}^2 \times \mathbb{E}^2 \times \mathbb{H}^2$ in an 8-class regression setting (analogous to the multi- K benchmark in Tables 2 and 3, varying one parameter at a time. Results are plotted in Figure 7.



(a) Changing the number of features seen by each DT/RF from 6 to 9 by including the (x_1, x_2) angle is massively beneficial.

(b) Changing feature subsampling approaches in RFs doesn't appear to do much.

(c) Increasing the maximum depth of each DT/RF is massively beneficial, and shows no signs of overfitting even at unrestricted max depth. All within-predictor differences are significant.

(d) Replacing the midpoint-angle computations with arithmetic means has no statistically significant effect on performance for DTs or RFs, surprisingly.

Figure 7: Effects of various hyperparameters on the performance of our algorithms. Asterisks imply that a result is statistically significant, as determined by the Wilcoxon test with a Bonferroni correction applied; asterisks are omitted for subfigure c, where all changes in depth are significant.

G. Detailed results

G.1. Global temperature prediction plots

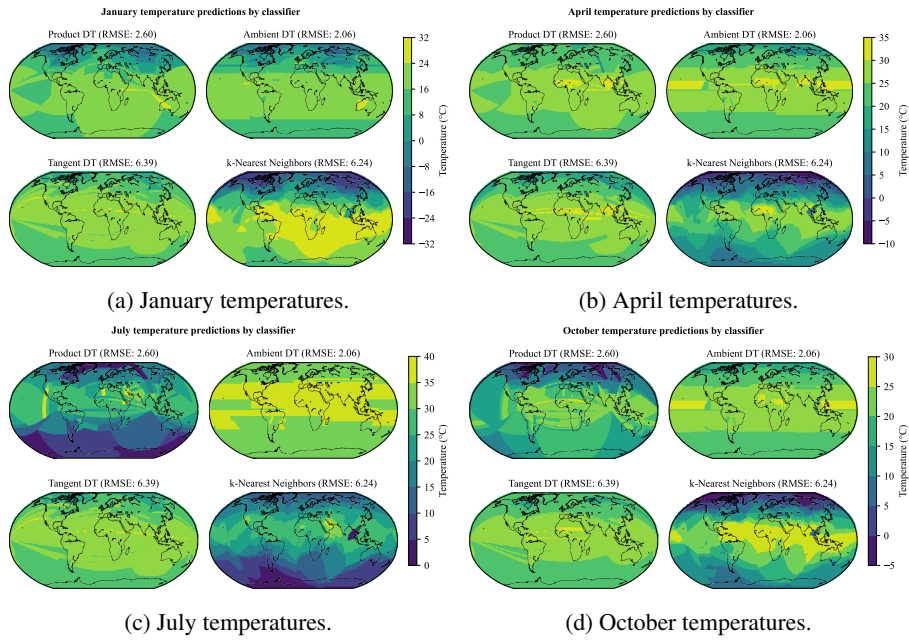


Figure 8: Decision boundaries for the temperature prediction task for the months of January, April, July, and October, colored by predicted temperature across four trained predictors.

G.2. VAE latent space visualizations

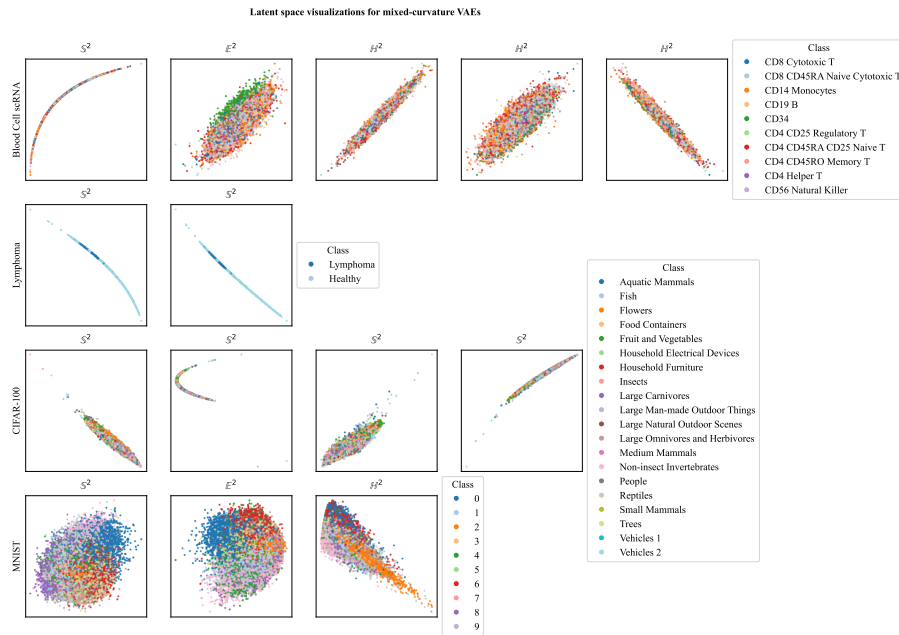


Figure 9: Visualizations of the latent space for all four of the datasets we embed using a VAE, colored by class. For visualization purposes, we show S^2 components in 2-dimensional polar coordinates, and project H^2 embeddings to the Poincaré disk.

H. Runtimes and complexity

We summarize complexities for models used in this paper, as well as the pairwise distance preprocessing necessary for operations such as computing nearest neighbors and creating reasonable graph edges for GNNs, in Table 7. Complexity estimates are adapted from Virgolin (2021).

To see that the training time complexity of ProductDT is $O(Dnd)$, observe that we must first preprocess the data into angles, which takes $O(nd)$ operations. From there, the angular comparison is a constant-time modification to the decision tree algorithm, so the complexity of ProductDT is $O(nd + Dnd) = O(nd)$. For inference, asymptotic performance is slightly slower than decision trees because preprocessing an input requires $O(d)$ operations.

If using all $\binom{d}{2}$ 2-D projections, training time complexities are all multiplied by d , and the $O(d^2)$ preprocessing step is added to test time complexities.

Table 7: Complexity comparison of machine learning models where: n : number of samples, d : number of features, h : neurons per layer, L : number of layers, D : maximum tree depth, s : number of support vectors. We include the complexity of computing pairwise distance, which are necessary for operating models like k -nearest neighbors and GNNs without topologies, as well.

Model	Phase	Time		Space	
		Worst	Avg	Worst	Avg
Dists		n^2d	n^2d	n^2	n^2
MLP	Train	$ndh + Lnh^2$	$ndh + Lnh^2$	$nd + dh + L(h^2 + nh)$	h^2L
	Test	h^2L	h^2L	h^2L	h^2L
Perceptron	Train	nd	nd	d	d
	Test	d	d	d	d
SVM	Train	n^3d	n^2d	n^2	n^2
	Test	sd	sd	sd	sd
GNN	Train	n^2d	n^2d	n^2	n^2
	Test	n^2	n^2	n^2	n^2
k-NN	Train	1	1	nd	nd
	Test	$nd + n \log n$	$\log n$	nd	nd
Decision Tree	Train	Dnd	Dnd	2^D	2^D
	Test	D	D	1	1
ProductDT (vanilla)	Train	Dnd	Dnd	2^D	2^D
	Test	$d + D$	$d + D$	d	d
ProductDT ($\binom{d}{2}$ splits)	Train	Dnd^2	Dnd^2	2^D	2^D
	Test	$d^2 + D$	$d^2 + D$	d^2	d^2

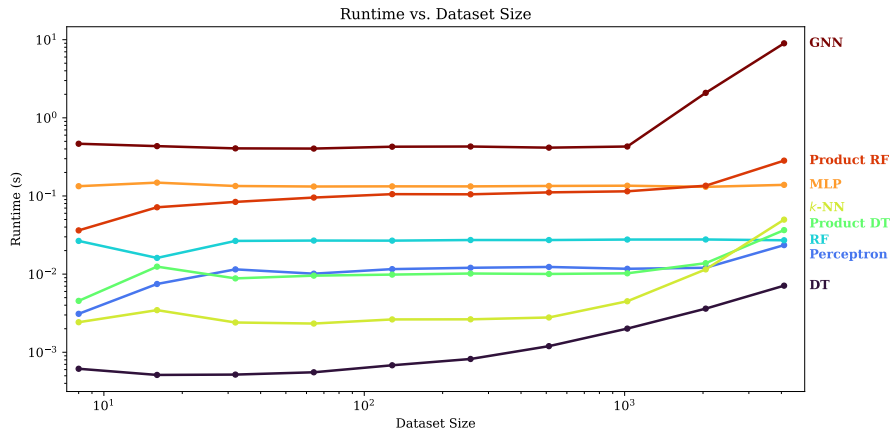


Figure 10: Runtime comparison for all of our methods

I. Interpretability and visualization

Alongside their demonstrated accuracy and efficiency, decision tree algorithms are attractive for their tractability and interpretability. In particular, given a trained decision tree \mathcal{T} , it is possible to:

1. Predict its behavior on the entire space of possible inputs (equivalently: \mathcal{T} partitions \mathcal{P} in a tractable way).
2. Determine the importance of features (for classic decision trees) or feature pairs/components (for ProductDT) by observing how often and how early a feature(/pair/component) is used in the decision tree procedure. Heuristically, early-splitting features are more important.
3. Visualize every node using a 2-dimensional projection of the input data and angle

I.1. Submanifold-level attribution experiment

To determine whether our method could accurately distinguish between relevant and irrelevant submanifolds, we drew independent samples from Gaussian mixtures in \mathbb{H}^2 , \mathbb{E}^2 , and \mathbb{S}^2 , and yielding datasets $(\mathbf{X}_{\mathbb{H}}, \mathbf{y}_{\mathbb{H}})$, $(\mathbf{X}_{\mathbb{E}}, \mathbf{y}_{\mathbb{E}})$, $(\mathbf{X}_{\mathbb{S}}, \mathbf{y}_{\mathbb{S}})$. We then concatenated these embeddings together:

$$\mathbf{X}_{\mathcal{P}} = \mathbf{X}_{\mathbb{H}} \oplus \mathbf{X}_{\mathbb{E}} \oplus \mathbf{X}_{\mathbb{S}}. \quad (83)$$

We trained three separate decision tree models on $\mathbf{X}_{\mathcal{P}}$, using $\mathbf{y}_{\mathbb{H}}$, $\mathbf{y}_{\mathbb{E}}$, and $\mathbf{y}_{\mathbb{S}}$ as labels. Because the labels and embeddings were drawn independently, it should be the case that only the component from the same manifold as the labels contains any relevant information, and the other two components are simply noise. Therefore, measuring the fraction of splits that fall in the “correct” manifold is a useful proxy for understanding tree models’ ability to pick out signal that happens in individual component manifolds.

Our results are summarized in Table 8. We found that both product space and ambient decision trees perform well at this task, which is to be expected.

We note that this analysis is unique to tree methods, where the split dimensions are part of the architecture; other methods, such as perceptrons, k -nearest neighbors, or neural networks are harder to query for feature(/component) importances. Therefore, we consider this simple experiment a useful demonstration of how decision tree learning can reveal aspects of structure in mixed-curvature datasets that other learning algorithms cannot reveal.

Table 8: Interpretability outcomes for Gaussian mixture. Percentages reflect the proportion of splits in the trained decision tree which fell in the non-spurious component manifold.

Model	\mathbb{H}^2	\mathbb{E}^2	\mathbb{S}^2
Product DT	100%	83%	86%
Ambient DT	100%	83%	67%

I.2. Visualization

A trained tree gives us all of the information we need to visualize the data and how it is split at every node, since each node looks at a 2-dimensional projection. We display three levels of a decision tree with a max depth of 3 in Figure 11. Note that, in this case, the decision tree also gives us relevant information about which 2-dimensional projections are worth looking at on the basis of their feature importances.

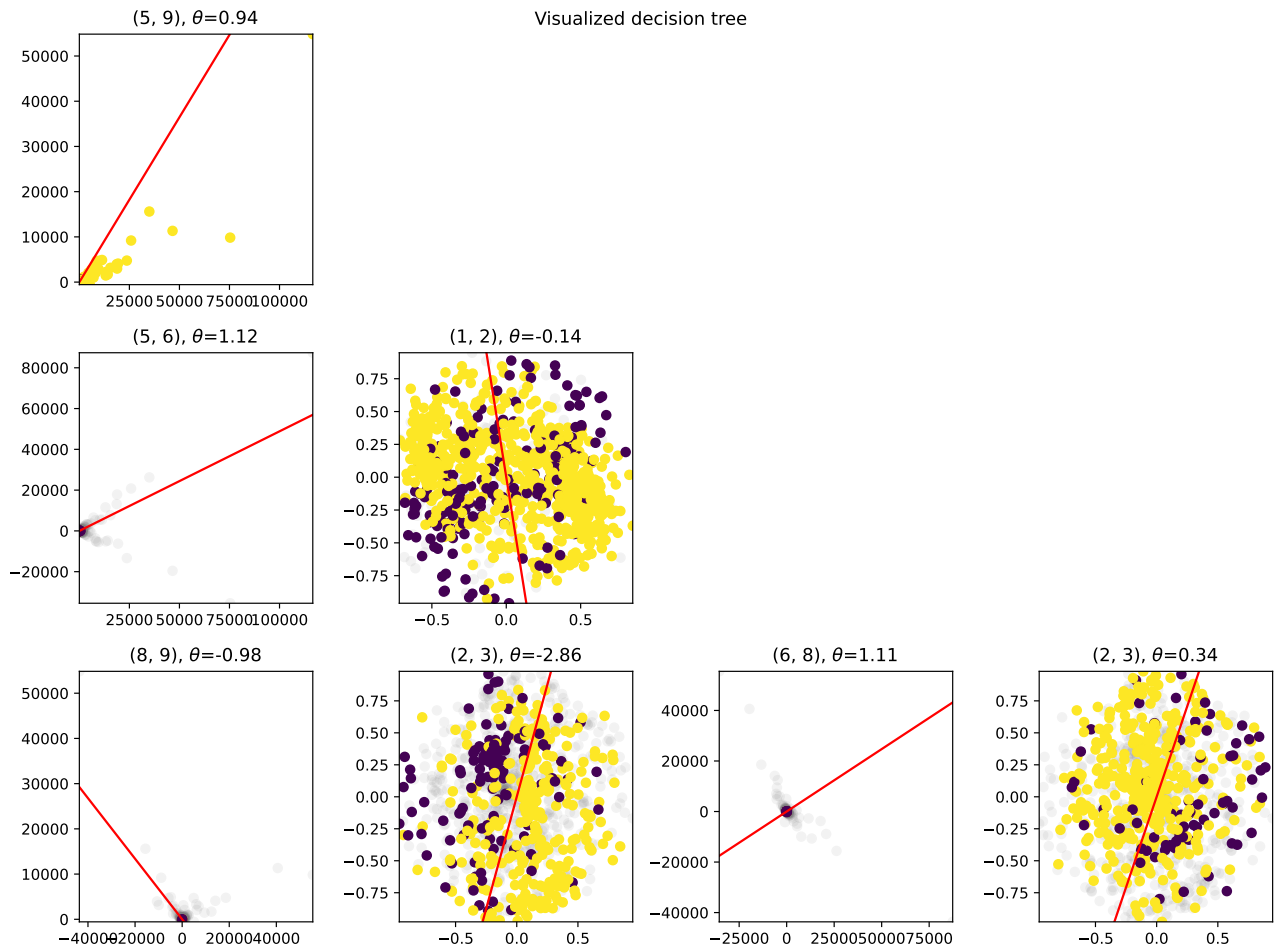


Figure 11: An example of a visualized decision tree for a Gaussian mixture in $\mathcal{P} = \mathbb{S}^4\mathbb{H}^4$. Greyed-out points are discarded “earlier” in the tree.

J. Datasets availability

Table 9: All of the datasets used in this paper, with download links and citations. CC-BY-SA is short for the Creative Commons Attribution-ShareAlike license. Allen TOU is the Allen Institute terms of use, found at <https://alleninstitute.org/terms-of-use/>.

Dataset	Link	License	Citation
CiteSeer	Network Repository: CiteSeer	CC-BY-SA	Giles et al. (1998)
Cora	Network Repository: CORA	CC-BY-SA	Sen et al. (2008)
Polblogs	Network Repository: Polblogs	CC-BY-SA	Adamic & Glance (2005)
CS PhDs	Pajek datasets: PhD students in CS	CC-BY-SA	Johnson (1984)
Adjnoun	Network Repository: Adjnoun	CC-BY-SA	Newman (2006)
Dolphins	Network Repository: Dolphins	CC-BY-SA	Lusseau et al. (2003)
Football	Network Repository: Football	CC-BY-SA	Girvan & Newman (2002)
Karate Club	Network Repository: Karate	CC-BY-SA	Zachary (1977)
Les Mis	Network Repository: Les Mis	CC-BY-SA	Knuth (1993)
Polbooks	Network Repository: Polbooks	CC-BY-SA	Krebs (2004)
Blood	10x Genomics: CD8+ Cytotoxic T-cells	CC-BY-SA	Zheng et al. (2017)
Blood	CD8+/CD45RA+ Naive Cytotoxic T Cells	CC-BY-SA	Zheng et al. (2017)
Blood	10x Genomics: CD56+ Natural Killer Cells	CC-BY-SA	Zheng et al. (2017)
Blood	10x Genomics: CD4+ Helper T Cells	CC-BY-SA	Zheng et al. (2017)
Blood	10x Genomics: CD4+/CD45RO+ Memory T Cells	CC-BY-SA	Zheng et al. (2017)
Blood	10x Genomics: CD4+/CD45RA+/CD25- Naive T cells	CC-BY-SA	Zheng et al. (2017)
Blood	CD4+/CD25+ Regulatory T Cells	CC-BY-SA	Zheng et al. (2017)
Blood	10x Genomics: CD34+ Cells	CC-BY-SA	Zheng et al. (2017)
Blood	CD19+ B Cells	CC-BY-SA	Zheng et al. (2017)
Blood	10x Genomics: CD14+ Monocytes	CC-BY-SA	Zheng et al. (2017)
Lymphoma	Hodgkin’s Lymphoma, Dissociated Tumor: Targeted, Immunology Panel	CC-BY-SA	10x Genomics (2020a)
Lymphoma	PBMCs from a Healthy Donor: Targeted-Compare, Immunology Panel	CC-BY-SA	10x Genomics (2020b)
MNIST	HuggingFace: MNIST	MIT	Lecun et al. (1998)
CIFAR-100	HuggingFace: CIFAR-100	None	Krizhevsky (2009)
Landmasses	Basemap 1.4.1: is_land	None	None
Neurons	Allen Brain Atlas	Allen TOU	Jones et al. (2009)
Temperature	Wikipedia: List of cities by average temperature	CC-BY-SA	Wikipedia (2024)
Traffic	Kaggle: Traffic Prediction Dataset	None	Fedesoriano (2020)